Acoustics Australia
https://doi.org/10.1007/s40857-026-00384-4

ORIGINAL PAPER

Broadband Sound Absorption with Low-Perforation Micro-Perforated Panels Coupled with Space-Coiling and Helmholtz Resonators: Numerical and Experimental Study

Emad Panahi[1] · **Francesco Braghin**[1] · **Alberto Corigliano**[2] · **Luca Sangiuliano**[3] · **Luca D'Alessandro**[3]

Received: 31 December 2025 / Accepted: 7 April 2026

Abstract

This study proposes a new sound absorbing panel designed for broadband low-frequency performance. The panel integrates a fixed low perforation rate micro-perforated panels (MPPs) with space-coiling and Helmholtz resonator slit-type structures, forming single- and double-layer units capable of wideband absorption. A hybrid series–parallel configuration, investigated using finite element analysis (FEA), creates multiple resonance peaks and enhances absorption bandwidth across low, mid, and high frequencies. To get optimum efficiency, a genetic algorithm (GA) is employed to optimize key geometric parameters. Experimental tests are conducted on both unoptimized and optimized prototypes, each with a 41 mm air cavity. The unoptimized design provides an absorption bandwidth of 1250 Hz (350–1600 Hz), while the optimized panel extends this slightly to 1255 Hz (345–1600 Hz). The Impedance tube measurements were validated against numerical predictions and, with the optimum design having a bandwidth-to-thickness ratio of 30.60 and being excellent performance than current absorbers documented in the literature. The proposed sound absorbing panel is thin and lightweight, making it particularly suitable for applications where weight and space constraints are critical, such as aerospace, civil engineering, and transportation, while providing a compact and practically feasible solution for broadband passive noise control.

Keywords Micro-perforated panel (MPP) · Helmholtz resonator (HR) · Broadband sound absorption · Acoustic metamaterial · Space-coiling structure · Genetic algorithm optimization

1 Introduction

Low-frequency noise has been a long-standing environmental problem, primarily in the cities. Road traffic, airplanes, machines, windmills, and ventilation systems are some of the common sources of noise [1]. Noise pollution is more severe in character since it has the potential to have a range of adverse impacts, such as stress, annoyance, fatigue, and sleep disturbance. One of the most controversial features of low-frequency noise is that it can go long distances with less or no attenuation in its energy [2]. Because of its frequency and effect, the control of low-frequency noise has become even more necessary and is still one of the key challenges in passive noise controlling [3]. Traditional sound-absorbing materials like porous foams and fibrous structures need sizable thickness in relation to the wavelength of the sound itself to be effective for sound absorbing [4]. In other words, conventional materials for blocking low-frequency noise are often bulky and difficult to install in compact applications [5].

This challenge led to the development of micro-perforated panels (MPPs), which have been regarded as a next-generation solution for sound absorption [6]. Micro-perforated panels (MPPs) feature precisely engineered tiny holes that dissipate sound energy by creating airflow resistance, converting it into a small amount of heat. Unlike traditional porous absorbers, which are often based on fibrous or foam materials with limited mechanical and fire resistance, MPPs are typically fabricated from solid materials, providing improved structural durability and enhanced flame resistance while offering mid-to-high frequency sound absorption [7]. The main limitation of traditional micro-perforated panels at

✉ Emad Panahi
emad.panahi@polimi.it

[1] Department of Mechanical Engineering, Politecnico Di Milano, 20156 Milano, Italy

[2] Department of Civil and Environmental Engineering, Politecnico Di Milano, 20133 Milano, Italy

[3] Phononic Vibes S.R.L., 20083 Milano, Italy

low frequencies is their narrow effective range, due to their inherent resonance characteristics. To address this, scholars have explored methods to extend their performance across a relatively large frequency spectrum [8, 9]. To overcome this limitation, researchers have tested combining multiple micro-perforated panels in various formations such as series, parallel, or hybrid series-parallel arrangements among different studies [10–12]. By means of multiple layers of micro-perforated panels in a parallel configuration significantly enhances sound absorption across a wide frequency range by introducing additional resonance peaks [13]. Subsequent studies have approved that the multilayer approach with using multiple perforation rate properties effectively covers low to high frequencies [14, 15]. However, adding more layers expands the overall thickness and can make the design bulky, as well as usage of different perforation rates, posing challenges for practical applications [1, 16].

An alternative approach to reducing low-frequency noise involves the use of acoustic metamaterials, which leverage localized resonances to absorb sound even when the structure is much smaller than the sound's wavelength. Techniques such as space-coiling structures and Helmholtz resonators achieve this by trapping and dissipating sound energy within specially designed structures [17–19]. Helmholtz resonators (HRs) are highly effective at reducing low-frequency noise, particularly at specific resonant frequencies. They function by using a small air cavity connected to a narrow neck or tube to trap sound waves, converting them into heat and thereby diminishing their intensity. Numerous investigations have pointed out that by adjusting the size, shape, and positioning of HRs, they can be precisely tuned to target different types of noise in various situations [20–23]. Integrating built in apertures into Helmholtz resonators has significantly simplified to reach the compact design of metamaterial units, driving increased research into developing and optimizing compact acoustic metamaterials based on this concept. However, despite the advantages, incorporating different aperture/neck shapes can still complicate the overall structure of sound absorbers [24–26].

A recent study in [27] introduced a compact acoustic metamaterial that uses Helmholtz resonators with side slits to address low-frequency noise. These side slits not only streamline the design but also provide greater flexibility in tuning the acoustic response. By varying the resonator depths across twenty-five units, the structure effectively absorbs sound within the 470–930 Hz range. The proposed model has shown a promising alternative to traditional Helmholtz resonators, as it can be easier to manufacture and allow fine-tuning of absorption peaks in the low-frequency region, however, when used solitary absorbing mechanism, its sound absorption range remains limited. To improve sound absorption while keeping the structure as thin as possible, space-coiling designs have been commonly employed. Nevertheless, these structures typically absorb sound over a limited frequency range, which often necessitates arranging a large number of units to achieve broader spectrum [28–30]. Among such designs, micro-perforated panels (MPPs) with coiled-up channels are remarkably widespread [31, 32]. Their frequency range is primarily determined by the total length of the coiled-up channels, which helps balance acoustic impedance at low frequencies by compensating for the resistance caused by the using multiple and separate perforation rates [33]. On the other hand, achieving effective absorption across low and wide frequency ranges using ultra and high perforation rate of MPPs combined with coiled-up channels still demands considerable structural thickness [34, 35].

To accomplish effective low-frequency noise reduction over a broad range, researchers have explored hybrid sound absorbers that combine multiple resonant modes. A common strategy involves arranging various resonant structures in series, such as multilayer Helmholtz resonators [36, 37], multilayer micro-perforated panels with not a fixed perforation rate properties [38], decorated membranes with air chambers [39, 40], and combinations of HRs and MPPs with elastic membranes and porous materials [41, 42]. Further approach uses series-parallel configurations of MPPs and HRs [43, 44]. In [45], researchers explored combining micro-perforated panels (MPPs) with Helmholtz resonators featuring inserted necks in both series and parallel configurations to enhance sound absorption. The findings revealed that this hybrid design significantly reduces the overall absorber thickness. Specifically, the combined HRIN–MPP structure achieved effective absorption between 318 Hz and 880 Hz with a thickness of 56 mm, although the series configuration exhibited pronounced anti-resonance effects. Followed by, in [46] three sound absorbers were developed using cavity-based designs, an MPP with an integrated Helmholtz resonator and single- and double-layer cavity-backed MPPs. Their acoustic performance, influenced by cavity partitions, was analysed using finite element analysis and optimized through particle swarm optimization procedure. Experimental results exhibited that the first mechanism achieved a half-bandwidth of 1294 Hz approximately 500 Hz wider than a standard MPP. The second and third optimized sound absorbing mechanisms provided absorption ranges of 794–1614 Hz and 632–1954 Hz, respectively. Previous studies have shown that combining micro-perforated panels (MPPs) with Helmholtz resonators simultaneously not only enhances mid- to high-frequency absorption but also effectively addresses low frequencies. However, many existing designs particularly those that rely on creating multiple absorption peaks face trade-offs such as increased thickness, use of high or multiple perforation rate properties, and limited operational bandwidth when attempting to reduce panel thickness. These challenges draw attention to a potential for developing a new panel that uses a fixed low-perforation-rate MPP combined with complementary sound-absorbing mechanisms to achieve low broadband frequency sound absorption while maintaining a compacted structure.

To address this research gap, the present work proposes a novel hybrid sound absorbing panel (SAP) composed of double- and single-layer units of MPPs which integrated by HR slit type, normal, and coiled-up space channels arranged in a series-parallel configuration. On the one hand, integrating MPPs with HR slit-type units in series as double-layer structures can improve the low and also maintain the high-frequency region operation thanks to their natural resonances behaviour, on the other hand, using MPP units with normal and coiled up space backing channels introduces multiple resonances by variation of the channels depth which can be compensated the anti-resonance effects between the low to mid and mid to high frequencies resulting in broader low-frequency sound absorption within the target range. Furthermore, the key parameters influencing the panel's full width at half maximum of the absorption coefficients (half-bandwidth) have been fine-tuned using a finite element analysis (FEA)-based genetic algorithm in COMSOL Multiphysics. Experimental validation for the optimized case confirmed that the suggested sound absorbing panel achieves a valuable sound absorption between 345 Hz and 1600 Hz, with a bandwidth-to-thickness ratio of 30.60, while preserving a fixed low perforation rate and a compact air cavity depth of 41 mm.

The paper is organized as follows: Section 2 introduces the sound absorbing panel design and 3D FEA simulation relations for calculating sound absorption. Section 3 exhibits in detail numerical analysis of the sound absorbing panel. Section 4 shows optimal sound absorption coefficients of the absorber through GA optimization technique. Section 5 provides experimental verification, and Section 6 concludes with key findings.

2 Material and Method

2.1 Sound Absorbing Panel Design

Studies in [43–46] have shown that combining a Helmholtz resonator (HR) with micro-perforated panels (MPPs) in a series–parallel arrangement improves sound absorption across low to high frequencies. However, varied HR aperture shapes and multiple perforation rates, while enhancing low-frequency performance, increase manufacturing complexity and introduce anti-resonances while used solitary reduce broadband sound absorption effect when a compacted panel size is needed. This study proposes a compact design with minimal air-cavity thickness that achieves efficient, wide bandwidth sound absorption while overcoming such drawbacks. As shown in Fig. 1, the proposed sound absorbing panel (SAP) comprises the nine units in three parallel rows which are repeated to fit as a 110 × 110 mm standard square type panel for practical application. The nine units consists of three double-layer units combining a fixed low-perforation-rate micro-perforated panel (MPP) and Helmholtz resonator slit-type (HRS) in series, paired in parallel with six single-layer units backed by normal and space coiling channels to enhancing low-frequency broadband absorption and delivering multiple peaks across 300–1600 Hz. Detailed numerical analysis and the idea's development are provided in Sect. 3. This section outlines the general design concept, with Fig. 1 presenting a schematic of the unoptimized proposed sound absorbing panel (SAP). The double-layer section features a micro-perforated panel (MPP) on the top surface, followed by a normal backing cavity as the first layer. The second layer incorporates a Helmholtz resonator slit type (HRS) with a rectangular neck and aperture. All three double-layer units share this structural arrangement but vary in the aperture height (h_{HRS}) and width (d_{HRS}) of the HRS. In contrast, the single-layer section consists of MPPs backed by either normal or space-coiling channels.

Figure 1 (a) presents the y–z plane cross-section and geometric details of all units. The proposed MPP features a fixed low perforation ratio of 0.6 % with narrow holes (0.3 mm) and a thin thickness (0.2 mm), narrow holes allowing more air and, consequently, more sound to pass into the backing cavity channel. This enhances the interaction between the panel and incident sound waves, broadening the high-frequency sound absorption bandwidth. Behind the MPP, the Helmholtz resonator slit type (HRS) serves as a second layer, with tuneable design variables to target specific low-frequency bands. Positioned after the MPP, it acts as a secondary sound trap, capturing energy that passes through the first layer. Since the MPP's shallow cavity depth and small holes do not absorb much long-wavelength energy, more low-frequency energy reaches to the HRS. As well, to reduce anti-resonances and capture residual sound energy across low–mid and mid–high frequency bands, MPPs coupled with normal and space coiling channels are employed. These channels can be tuned by adjusting their equivalent resonator length, enabling control over the absorption coefficients.

Additionally, Fig. 1 (a) illustrates that the width and height of the coiled-up spaces, the height of the normal channels, and the aperture dimensions of the HRS units are defined as adjustable geometric parameters within the design framework and enabling systematic tuning during the optimization process. This tunability provides the ability to have a variable cross-sectional path for the propagation of sound waves. Likewise, Fig. 1 (b) illustrates the 3D decomposition of the air region of the proposed sound absorbing panel (SAP). The perforation and the slit area have been

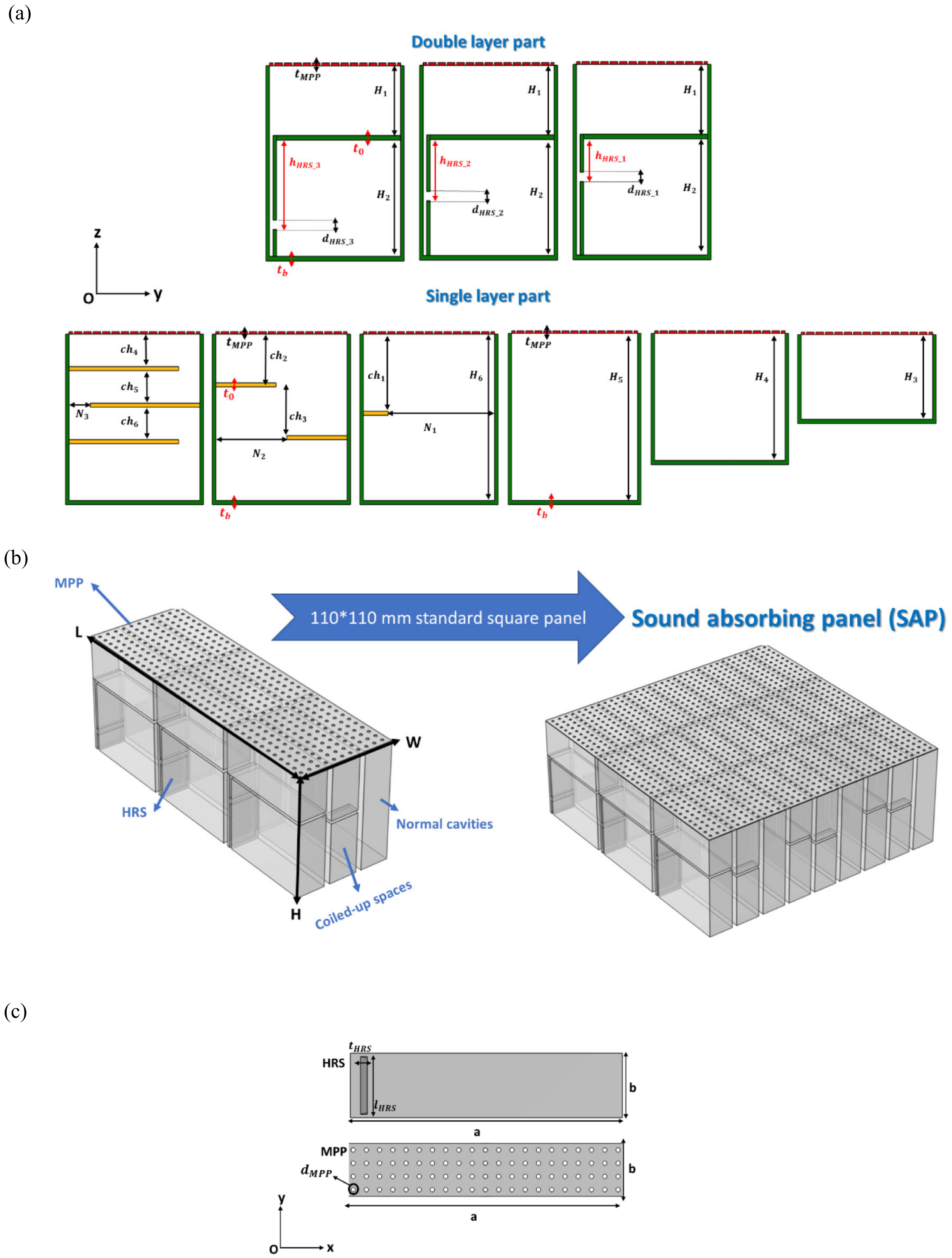

Fig. 1 Geometric configuration of the sound absorbing panel (SAP): **a** cross-section of the proposed units individually in the y–z plane, **b** 3D perspective of the sound absorbing panel (SAP) with corresponding air domains, **c** close-up view of the micro-perforated plate (MPP) and HR slit type (HRS) geometrical properties

Table 1 Initial geometrical parameters, HRS and MPPs properties

Parameter	L	W	H	a	b	t_0	t_b	H_1	H_2	
Value	106 mm	34 mm	41.2 mm	36 mm	12 mm	1 mm	1 mm	15 mm	25 mm	
Parameter	H_3	H_4	H_5	H_6	N_1	N_2	N_3	ch_1	ch_2	
Value	20 mm	30 mm	41 mm	41 mm	30 mm	20 mm	6 mm	19 mm	12 mm	
Parameter	ch_3	ch_4	ch_5	ch_6	d_{HRS_1}	h_{HRS_1}	d_{HRS_2}	h_{HRS_2}	d_{HRS_3}	h_{HRS_3}
Value	12 mm	8 mm	8 mm	8 mm	2 mm	8 mm	2 mm	12 mm	2 mm	18 mm
HRS					MPP					
t_{HRS}(mm)	l_{HRS}(mm)				d_{MPP}(mm)	t_{MPP}(mm)		Perforation rate (%		
1	10				0.3	0.2		0.6		

shown in Fig. 1. (c), also respective characteristics of the unoptimized panel have been outlined in Table 1 together with other preliminary design parameters. It should be noted that the total air cavity depth of 41 mm results from the series combination of a 15 mm MPP backing cavity and a 25 mm HRS cavity, selected through preliminary parametric analysis to enable low-frequency resonance tuning under 350 Hz while maintaining a compact subwavelength thickness significantly smaller than conventional porous absorbers operating in the same frequency range [1–3].

2.2 Finite Element Analysis

Finite element analysis (FEA) is a widely used technique for evaluating the acoustic performance of coupled structures. Unlike theoretical models, acoustic FEA offers greater accuracy by more realistically representing the actual conditions of complex and integrated sound absorber systems [32, 34, 47]. For this reason, the sound absorption performance of the proposed sound absorbing panel (SAP) is assessed using a 3D FEA simulation approach. In this study, the simulation incorporates both acoustic pressure and thermo-viscous acoustics boundary conditions. The acoustic field has been modelled using the Helmholtz equation, as described in [48, 49]:

$$\nabla \cdot \left(-\frac{1}{\rho_0}\nabla p\right) - \frac{1}{\rho_0}\left(\frac{\omega}{c}\right)^2 = 0 \tag{1}$$

And acoustic pressure control equations in frequency domain are:

$$\nabla \cdot \left(-\frac{1}{\rho_c}q_d\right) - \frac{k_{eq}^2 p_t}{\rho_c} = Q_m \tag{2}$$

$$p_t = p + p_b \tag{3}$$

$$k_{eq}^2 = \left(\frac{\omega}{c_c}\right)^2 - k_z^2 \tag{4}$$

$$c_c = c, \quad \rho_c = \rho_0 \tag{5}$$

where ρ_0 represents the air density, p denotes the acoustic pressure, p_b corresponds to the background sound pressure. The angular frequency is given by ω, while c is the speed of sound, the dipole and monopole domain sources are defined as q_d and Q_m. The k_z describes the wave numbers outside the surface, which, were set to zero, additionally k_{eq} is the equivalent wave number. To account for thermal and viscous losses within the micropores and narrow channels, the Thermal-Viscous-Acoustic module has been employed [48, 49].

$$i\omega p_t + \nabla \cdot (\rho_0 u_t) = 0 \tag{6}$$

$$i\omega \rho_c u_t = \nabla \cdot \delta \tag{7}$$

$$\rho_0 C_p(i\omega T_t + u_t \cdot \nabla T_0) - \alpha_p T_0(i\omega p_t + u_t \cdot \nabla p_0) = \nabla \cdot (k\nabla T_t) + Q \tag{8}$$

$$\delta = -p_t I + \mu\left(\nabla u_t + (\nabla u_t)^T\right) - \left(\frac{2}{3}\mu - \mu_B\right)(\nabla \cdot u_t)I \tag{9}$$

$$\rho_t = \rho_0\left(\beta_T p_t - \alpha_p T_t\right) \tag{10}$$

Here, p_0 denotes the equilibrium pressure, T_0 is equilibrium temperature, and ρ_0 is equilibrium density. The total sound field velocity and total temperature field temperature are given by u_t and T_t, respectively. The specific heat ratio is defined as γ, while k stands for the thermal conductivity, μ is the dynamic viscosity, μ_B is bulk viscosity, and C_p corresponds to the heat capacity at constant pressure. Additionally, α_p and β_T are the coefficient of thermal expansion and the isothermal compressibility, respectively [48, 49]. These quantities are defined as follows:

$$\alpha_p = \frac{1}{c}\sqrt{\frac{C_p(\gamma - 1)}{T_0}} \tag{11}$$

$$\beta_T = \frac{1}{\rho_0}\frac{\gamma}{c^2} \tag{12}$$

Acoustic impedance implies to the ratio of the sound pressure and volume velocity of a medium over a specific area of the wavefront, which is expressed as:

$$Z_a = \frac{P}{U} \tag{13}$$

Here, Z_a signifies acoustic impedance,Pa.s$/m^3$; P is sound pressure, Pa; U denotes volume velocity, $U = S \times v$,m^3/S. The acoustic impedance is multiplied by the cross-sectional area to attain the specific acoustic impedance:

$$Z_s = S \cdot Z_a = \frac{P}{v} \tag{14}$$

When the sound wave is incident normally, the absorption coefficient of the proposed panel is given by:

$$\alpha = 1 - \left|\frac{Z_s - Z_0}{Z_s + Z_0}\right|^2 \tag{15}$$

where $Z_0 = \rho_0 c_0$ is the characteristic impedance in air, $\rho_0 = 1.21$ kg$/m^3$ is the density of air, and $c_0 = 343$ m$/s$ is the speed of sound in air.

To investigate sound wave propagation and energy dissipation in a background medium integrated with the proposed sound absorbing panel (SAP), numerical simulations were performed using COMSOL Multiphysics 6.2. The Pressure Acoustics and Thermal Acoustics modules were employed to model the panel and its unit structures, following the governing equations presented in Section 2.2. The numerical setup has been designed to reflect experimental conditions for evaluating sound absorption coefficients, as illustrated in Fig. 2. The finite element (FE) simulation involves a normally incident plane wave with a unit amplitude of 1 Pa, propagating in the z-direction and striking the panel. To model the panel, the micro-perforated plate on the panel's surface is represented using an interior perforated plate boundary condition, while all other components are explicitly modelled to enhance simulation accuracy.

The pressure acoustic field domain has been meshed with ten-layer swept meshes, whereas the remaining structural parts are discretized using free tetrahedral elements. For sufficient resolution, the smallest mesh element is set to one-tenth of the minimum wavelength considered. To capture thermo-viscous losses within the normal/coiled channels and Helmholtz resonator (HRS) cavities, six mesh layers are applied along the channel walls. These meshing strategies ensure accurate results with minimal computational cost. The thickness of each thermo-viscous mesh layer, d_v, is defined as: $d_v = \sqrt{2\eta/\rho_0\omega}$, which corresponds to the viscous boundary layer thickness. This allows proper resolution of acoustic damping effects near the channel walls, where viscous forces are dominant. Additionally, hard boundary conditions are applied at solid-air interfaces due to the large acoustic impedance mismatch between the solid materials and air. Finally, the sound absorption coefficient (α), is calculated either using Eq. (15) or defined as: $\alpha = 1 - \left|{p_{\text{scat}}}/{p_{\text{inc}}}\right|^2$ where p_{scat} is the total scattered pressure and p_{inc} is the total incident pressure.

3 Numerical Analysis of Sound Absorbing Panel

3.1 Double-Layer MPP Coupled by Normal Channel and HRS Unit

In the first part of this section, we analyse a single micro-perforated panel (MPP) with fixed properties and 15 mm air cavity size to examine how changing the cavity size influences its sound absorption spectrum while other MPP effective characteristics are restricted. Figure 3 shows how the changes in the MPP cavity size influence both the bandwidth and the magnitude of sound absorption in the mid- to high-frequency range. As illustrated in Fig. 3 (a), a single unit with a perforation ratio of 0.6%, hole diameter of 0.3 mm, and thickness of 0.2 mm achieves perfect sound absorption ($\alpha \geq 0.9$) at 1200 Hz. The full width at half maximum of the absorption peak defined as the effective bandwidth extends from 800 to 1600 Hz, resulting in a bandwidth of 800 Hz. This improved performance arises from the use of narrow micro-holes, a thin plate, and a low perforation ratio, which lead to a perforated constant of $1<K<4$, as noted in references [8, 9]. Such a configuration is advantageous for achieving efficient sound absorption in the target frequency range, specifically at the high region. Fig. 3 (b) further illustrates that increasing the MPP cavity size shifts the sound absorption performance towards lower frequencies (from 1600 to 715 Hz), while the bandwidth of sound absorption remains nearly unchanged. This indicates that by carefully adjusting the air cavity depth or equivalent length of a panel with fixed MPP properties and a compacted physical thickness, the effective sound absorption bandwidth can be maintained across a broad range of frequency. From the results of Fig. 3. (b), the cavity size of 15 mm has been selected as a first layer to be effective particularly at the high frequency region.

In the next part, as shown in Fig. 4, a single Helmholtz resonator slit type (HRS) unit with a 25 mm air cavity is analysed to investigate how variations in its geometric parameters affect the sound absorption coefficient. Owing to its

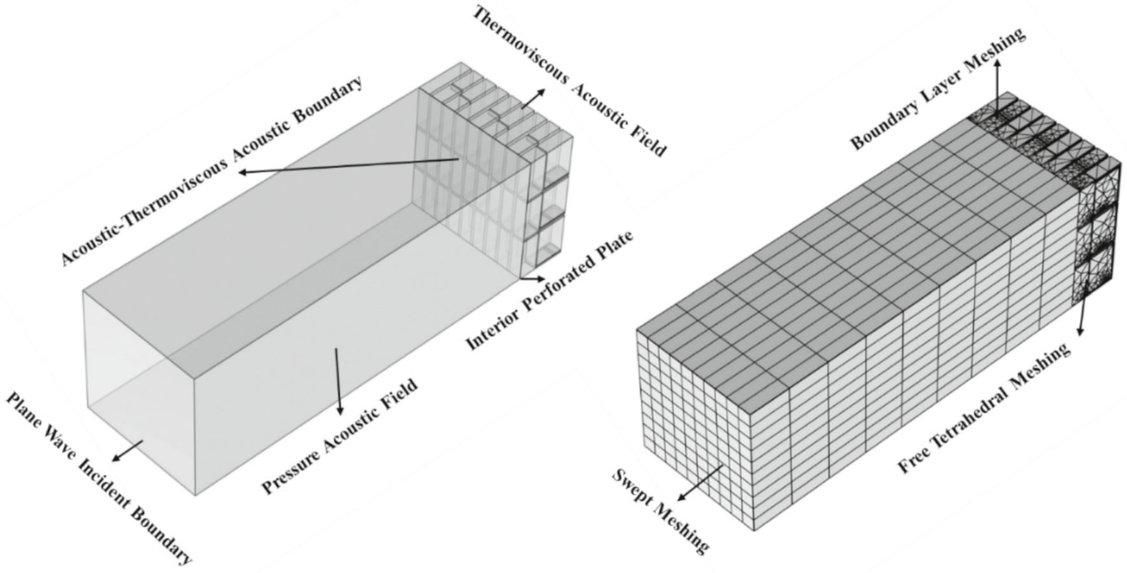

Fig. 2 Illustration for the FE simulation and meshing settings of SAP

resonance-based mechanism, the HRS performs most effectively in the low-frequency range. As illustrated in Fig. 4. (a), the HRS with a cavity height of 25 mm, an aperture height (h_{HRS}) of 18 mm, and an aperture width (d_{HRS}) of 2 mm reaches a quasi-perfect absorption ($\alpha \geq 0.8$) at 350 Hz, though this occurs within a narrow bandwidth of approximately 60 Hz. Fig. 4 (b) demonstrates that increasing h_{HRS} shifts the sound absorption spectrum towards lower frequencies, consistent with the trend seen in Fig. 4 (a). Conversely, as shown in Fig. 4 (c), reducing d_{HRS} also moves the absorption peak to lower frequencies.

The impact on the resonant frequency of the slit and aperture can be explained in a similar manner to a Helmholtz resonator with internally fabricated apertures [24–27]. In this analogy, the aperture width (d_{HRS}) corresponds to the aperture area in a standard HR, while the aperture height (h_{HRS}) is analogous to the neck length. Among these parameters, variations in h_{HRS} have a stronger impact on the resonant frequency than changes in d_{HRS}. Additionally, there is a clear trade-off between resonant frequency and bandwidth. This makes tuning the geometric parameters of the HRS unit an effective method for controlling resonance behaviour in the low-frequency region. Such tunability is especially useful when designing arrays of HRS units with closely spaced frequencies, as it allows more precise control over the targeted absorption range.

Now in the last part of this section, the two distinct features of the proposed MPP and HRS are combined in a series-connected configuration (MPPHRS), using the identical geometric parameters from the previous single layer cases, as illustrated in Fig. 5. (a). The resulting sound absorption curve shows that the double-layer unit, with a total cavity depth of 41 mm, produces two distinct peaks of perfect sound absorption ($\alpha \geq 0.9$) at 320 Hz and 1325 Hz. This dual-peak behaviour arises from the complementary characteristics of the two layers; the MPP with a normal channel dominates absorption in the high-frequency region, while the HRS unit enhances absorption in the low-frequency region. As shown in Fig. 5. (a), the series combination produces two distinct absorption bandwidths simultaneously in both the low- and high-frequency regions. Notably, the bandwidth in the low-frequency range is significantly broader than that achieved by the second layer alone, with the overall sound absorption performance also exhibiting a slight shift towards lower frequency.

This effect can be explained by the structural properties of the MPP and HRS. Owing to the narrow holes and thin thickness of the MPP at the top layer, high-frequency sound waves with relatively broad bandwidth are gradually dissipated, though with minimal attenuation in absorption. Following this, low-frequency sound energy is detected by the HRS unit, which is designed to be a dissipation system at its resonant frequency. These mechanisms combined reduce reflection and maximize absorption for both low- and high-frequency bands, a performance based on double-layer unit's relatively low surface impedance sensitivity [8, 9]. In the low band, half-bandwidth varies from 250 to 385 Hz, showing a width of 135 Hz, while in the high band from 985 to 1600 Hz, which is equivalent to 615 Hz. The direct contrast between double-layer and single-layer units reveals the principal advantage of the combined design, the low-frequency half-bandwidth is more than doubled (135 Hz compared with 60 Hz for the single HRS unit), but the wide high-frequency bandwidth is quite preserved. This result demonstrates an

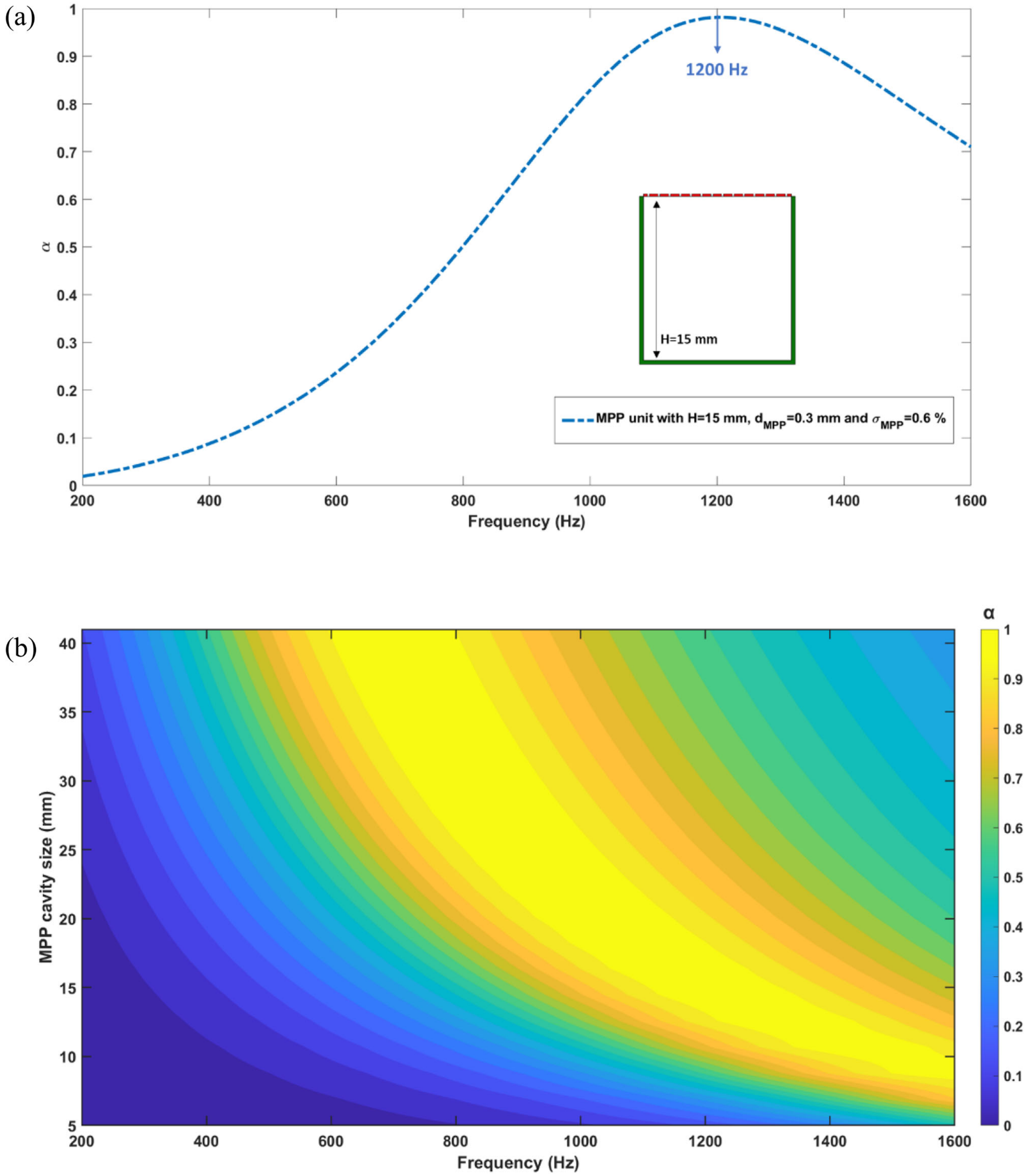

Fig. 3 Sound absorption coefficients of a single MPP unit with normal backed cavity **a** and effect of cavity height **b** variations on the sound absorption spectrum

Fig. 4 Sound absorption coefficients of a single HRS unit **a** along with effect of aperture height **b** and aperture width variations **c** on the sound absorption spectrum

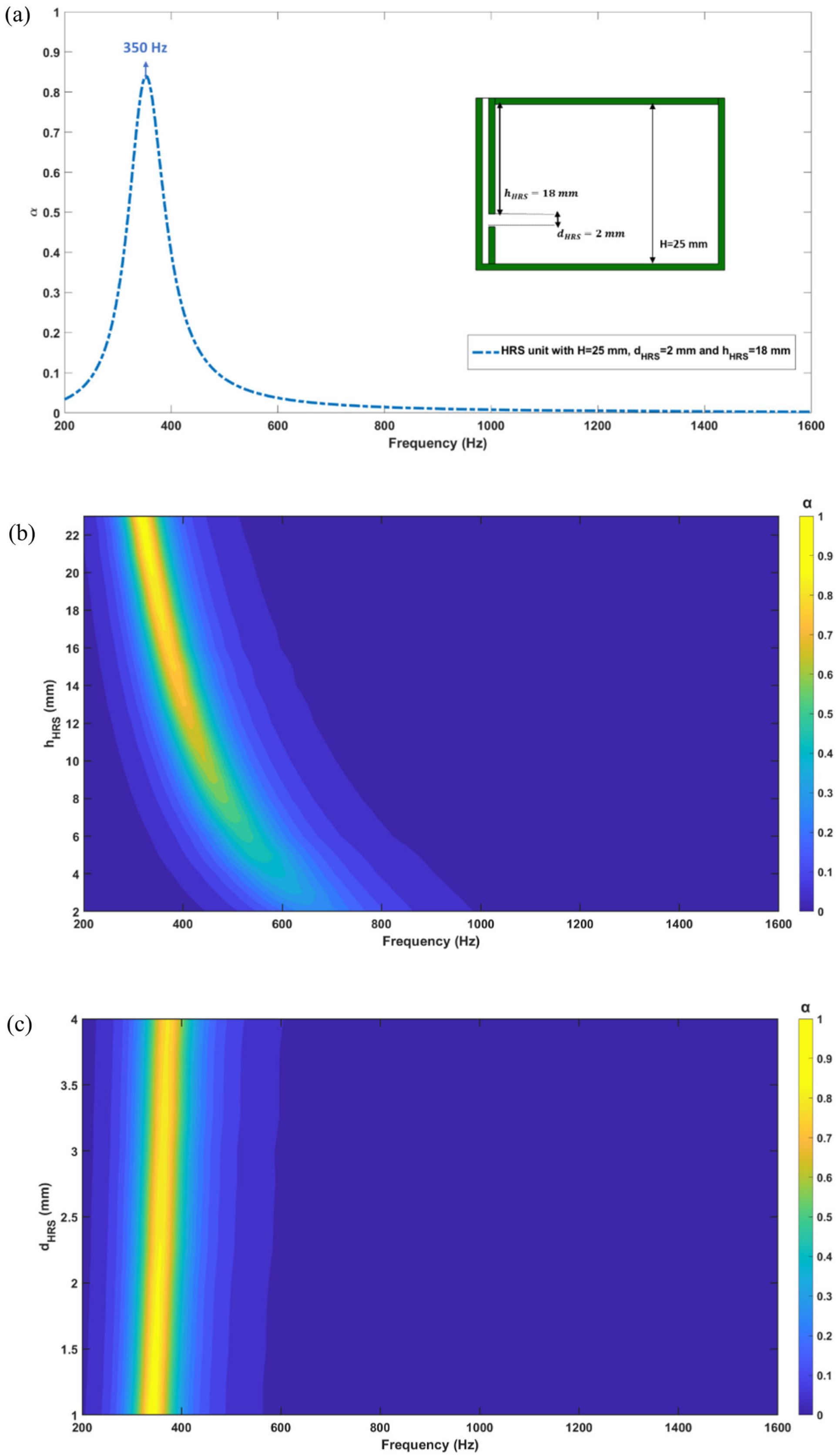

Fig. 5 Sound absorption coefficients of a single double-layer unit with MPP and HRS in series (MPPHRS) **a** along with effect of aperture width **b** and aperture height variations in the second layer **c** on the total sound absorption spectrum

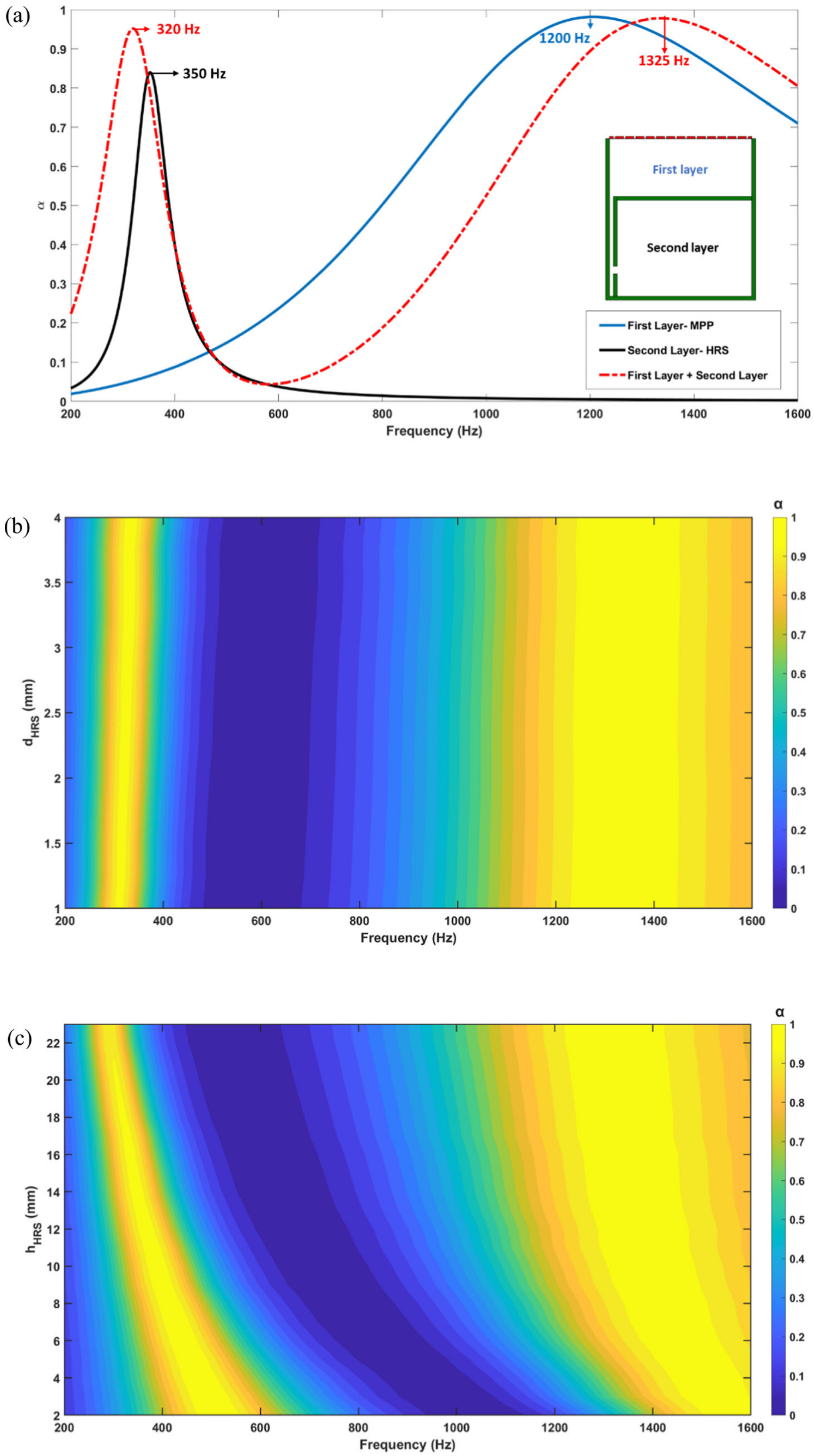

effective approach by applying a parallel arrangement to the double-layer unit, it is possible to achieve a broad sound absorption spectrum at the desired frequency, while also reducing the complexity of the used units and maintaining a fixed low perforation rate for practical applications.

Furthermore, Fig. 5 (b) and (c) has been analysed to gain insight into how variations in the second-layer geometrical parameters (d_{HRS} and h_{HRS}) influence the overall sound absorption spectrum of the double-layer unit. The resonance frequency in the lower region decreases as h_{HRS} increases. Conversely, reducing $\mathrm{d}_{\mathrm{HRS}}$ shifts the sound absorption peak towards the lower region, while simultaneously preserving a wide bandwidth at both low and high frequencies, along with stable quasi-perfect sound absorption coefficients ($\alpha \geq 0.8$). However, an open question remains, how can the dip in the mid-frequency range (600–1200 Hz) be addressed to achieve broadband sound absorption across the full spectrum; the analysis of Fig. 5. (b) and (c) suggests a promising approach, offering a way to overcome the limitations of low-frequency absorption while simultaneously maintaining quasi-perfect absorption in both low- and high-frequency ranges. The results obtained so far are insufficient solitary to improve performance in the mid-frequency range, as they fail to provide significant absorption peaks and effective bandwidth within this region, as clearly shown in Fig. 4. (b) and Fig. 5. (b-c). This limitation requires an alternative mechanism. In the next section, the idea of using a single-layer mechanism with MPPs integrated with normal (MPP) and space coiling channels (MPPSC) are presented to address this gap.

3.2 Single Layer MPP Unit Integrated by Normal and Space Coiling Channels

Consider a single-layer unit with a maximum air cavity depth of 41 mm, consisting of a micro-perforated plate with a fixed low perforation rate on top and backing made of normal or coiled-up space channels (see Fig. 1). As noted earlier, enhancing sound absorption curve from the low-to-mid and mid-to-high frequency range requires a mechanism that can both increase and stabilize absorption peaks across the regions. To achieve this, the performance of single-layer MPP units combined with normal and coiled-up space channels which having identical properties as listed in Table 1 has been studied in Fig. 6, with particular attention to their sensitivity across the operating frequency range. Figure 6 (a) shows the same performance as the result of Fig. 4. (b) with its limited operation range between 715 Hz and 1600 Hz with a perfect sound absorption ($\alpha \geq 0.9$); as illustrated utilizing the normal backing channel with different equivalent length cannot tackle alone the operation limitation below the 715 Hz, however, they can be useful for creating the absorption peaks between the mid to high frequency range. On the other side, to enhance the sound absorption frequency operation performance to lower region, the usage of the space coiling structures without increasing the physical air cavity size is great of importance.

The results in Fig. 6.(b) indicate that using coiled-up space resonators, which guide sound through variable cross-section channels, provides an effective mechanism for generating resonances and tuning the sound absorption values from the low to mid-frequency range by adjusting the panel's equivalent length. As shown in Fig. 6.(b), increasing the panel's equivalent length shifts the sound absorption performance from 715 Hz down to 400 Hz with achieving a perfect sound absorption ($\alpha \geq 0.9$). Importantly, this shift occurs without sacrificing the wide absorption bandwidth across both the low-to-mid and mid-to-high frequency ranges due to the utilizing different number of subchannel (see Fig. 1) with a fixed low perforation rate. Furthermore, as implied from Fig. 6.(a) and (b), achieving effective absorption across the target frequency range requires additional units alongside the double-layer units, with at least the equivalent lengths between 20 and 136 mm. These units are crucial for compensating the absorption dips in both the low-to-mid and mid-to-high frequency regions of the proposed sound absorbing panel (SAP). In the following section, based on the results of the current and the previous section, we present step-by-step development of the sound absorbing panel. This system is composed of series-parallel arrangements of single- and double-layer MPP units, integrated with normal channels, space coiling channels, and HRS.

3.3 Series-Parallel Coupling of MPPs Integrated by Normal, Space Coiling and HRS Units

As discussed in the previous section, incorporating both double- and single-layer units can demonstrate a strong potential for enhancing sound absorption across low, mid, and high frequencies when implemented in a compact panel. Achieving multiple resonance bands relies primarily on the parallel arrangement of these integrated units. Fig. 7. (a–c) explains the effects of coupling MPP, MPPSC, and MPPHRS units, each arranged in a three-unit parallel configuration. The 3D geometries of the normal, space coiling, and HRS units, along with the micro-perforated properties previously detailed in Fig. 1 and Table 1, have been used in the simulation model to calculate the sound absorption coefficients.

At the first place, Fig. 7 (a) presents the examination of three single-layer MPP units arranged in a parallel configuration. As shown in Fig. 7 (a), each unit contributes to the overall MPP coupled sound absorption spectrum, represented by the blue curve of the parallel combination. MPP-unit1, shown by the black curve, exhibits a dominant absorption peak with a perfect performance ($\alpha \geq 0.9$) at 715 Hz, along with a wide bandwidth spanning 400–1300 Hz. MPP-unit2,

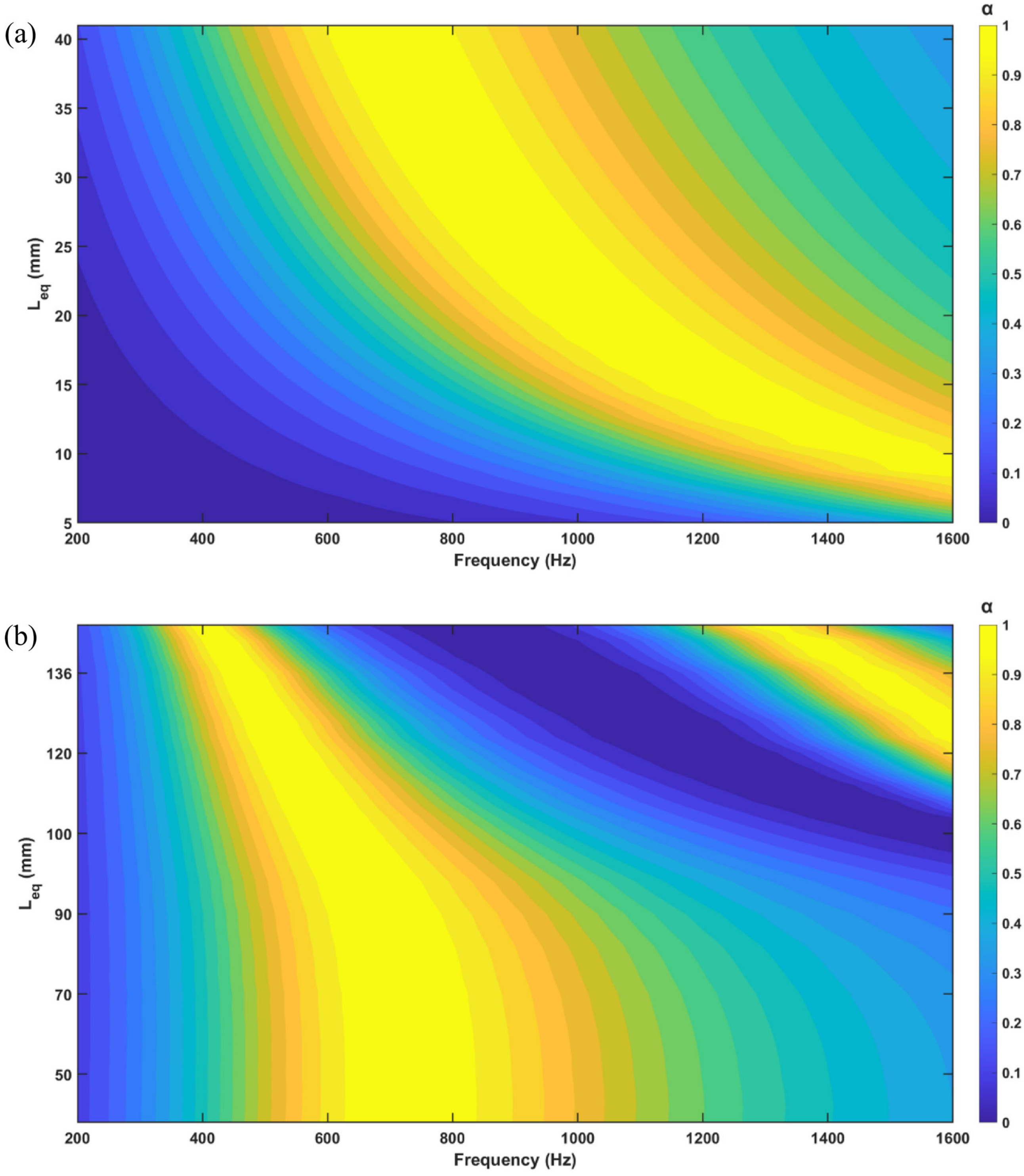

Fig. 6 Effect of equivalent length variations in MPP with normal **a** and space coiling backing channels (MPPSC) **b** on the sound absorption coefficients of a single layer unit

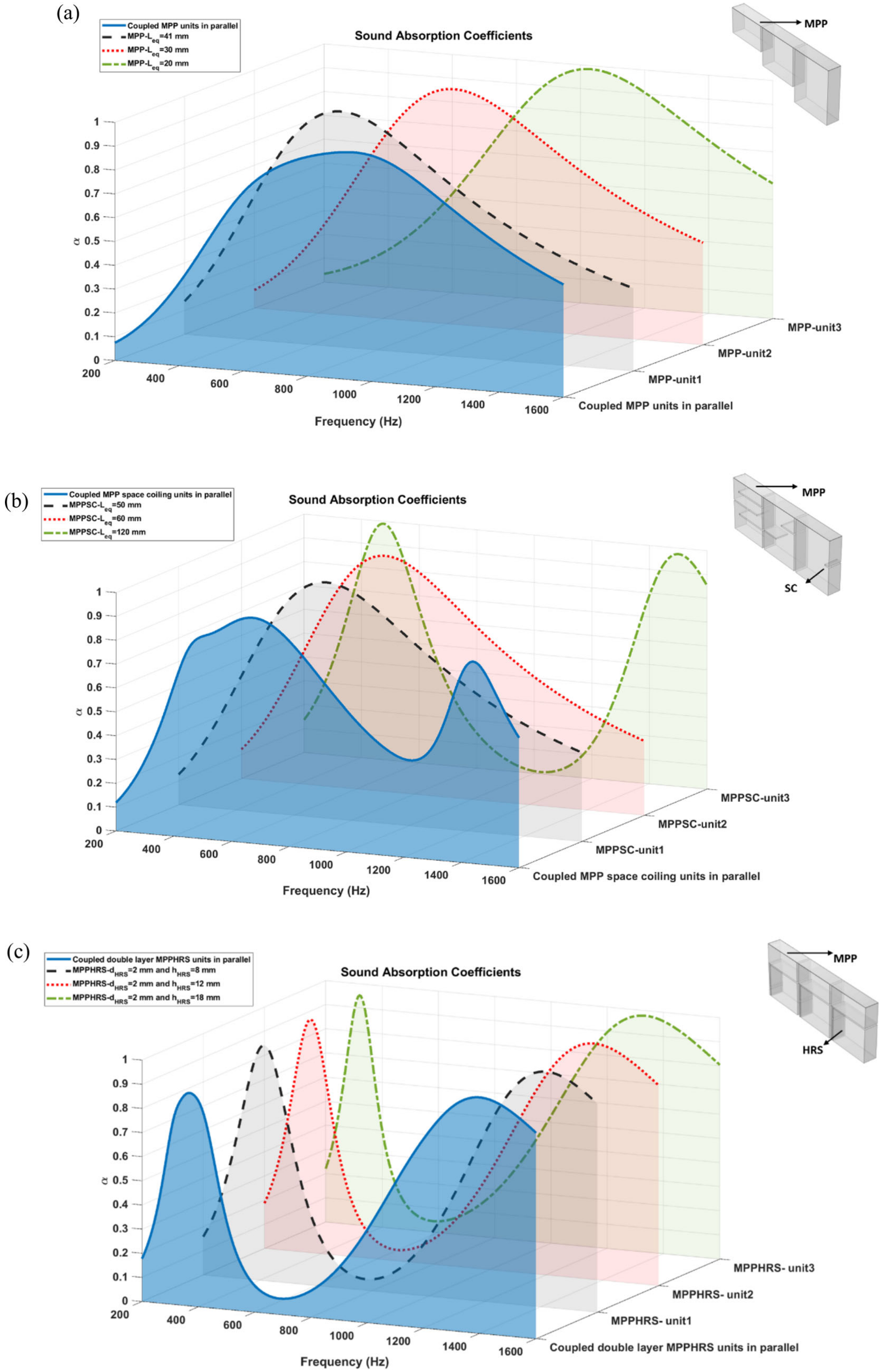

Fig. 7 Sound absorption performance of the unoptimized coupled three MPP (**a**), MPPSC (**b**), MPPHRS (**c**), and effect of each individual unit in a parallel connection

represented by the red curve, has a strong absorption peak at 800 Hz ($\alpha \geq 0.9$) and a wide absorption range from 490–1400 Hz. Similarly, MPP-unit3, indicated by the green curve, shows a leading peak at 1010 Hz ($\alpha \geq 0.9$), with a bandwidth extending from 660–1600 Hz. The combined response of the coupled MPP units, revealed by the blue region in Fig. 7. (a), produces three smooth absorption peaks with perfect performance ($\alpha \geq 0.9$) at 750 Hz, 850 Hz, and 950 Hz. This parallel configuration has created the half-bandwidth range from 475 to 1545 Hz.

In the second stage, three single-layer MPPSC units have been arranged in a parallel configuration. This setup has been introduced to achieve more lower frequency sound absorption compared to the normal MPP units. The parallel arrangement of the three coupled MPPSC units is illustrated in Fig. 7.(b). As illustrated in Fig. 7.(b), each unit contributes to the overall coupled MPPSC absorption spectrum, represented by the blue curve of the parallel combination. MPPSC-unit 1 (black curve) shows a main absorption peak with a perfect performance ($\alpha \geq 0.9$) at 695 Hz and a wide bandwidth spanning 395–1325 Hz. MPPSC-unit 2 (red curve) exhibits a strong peak at 680 Hz ($\alpha \geq 0.9$) with a bandwidth ranging from 390–1250 Hz. MPPSC-unit 3 (green curve) displays two perfect absorption peaks ($\alpha \geq 0.9$) at 470 Hz and 1500 Hz, with corresponding bandwidths of 340–640 Hz and 1330–1630 Hz. The double peaks arise from the increased equivalent length of 120 mm achieved through the use of four subchannels (see Fig. 1). The combined performance of the three coupled MPPSC units, shown by the blue area in Fig. 7.(b), results in three absorption peaks with a quasi-perfect performance ($\alpha \geq 0.8$) at 475 Hz, 670also creating two half-bandwidth ranges of

Hz, and 1440 Hz, also creating two half-bandwidth ranges of 370–1070 Hz and 1315–1630 Hz. As obvious from Fig. 7.(b), increasing the number of sub-channels extends the equivalent length, thereby shifting the sound absorption performance towards lower frequencies.

For the third step, the three coupled MPPHRS units comprising double-layer structures arranged in a parallel scheme have been considered, as shown in Fig. 7.(c). The MPPHRS units have designed based on the geometrical specifications presented earlier in Fig. 1 as the unoptimized units. Each unit consists of a first layer with a normal channel and a second layer integrated with an HRS unit but with different critical parameters, their geometrical parameters detailed in Table 1. From the initial look at Fig. 7.(c), each unit contributes to the overall coupled sound absorption spectrum, which represented by the blue curve of the double-layer MPPHRS configuration. MPPHRS-unit 1 exhibits two strong absorption peaks ($\alpha \geq 0.9$) at 410 Hz and 1410 Hz, with wide bandwidths spanning 310–530 Hz and 1120–1660 Hz. MPPHRS-unit 2 (red curve) also displays two dominant peaks at 360 Hz and 1360 Hz ($\alpha \geq 0.9$), with bandwidths ranging from 275–450 Hz and 1050–1630 Hz.

Likewise, the MPPHRS-unit 3 (green curve) archives two peaks at 320 Hz and 1325 Hz ($\alpha \geq 0.9$), accompanied by bandwidths of 250–385 Hz and 985–1600 Hz. These clearly reflect that with increase in aperture height (h_{HRS}) in the double-layer unit, peak frequencies reduce in both low- and high-frequency regimes. Consequently, the coupling behaviour of the MPPHRS units in Fig. 7.(c) (blue highlighted area), produces two dominant absorption peaks with perfect sound absorption ($\alpha \geq 0.9$) at 365 Hz and 1390 Hz; this broadens the low-frequency bandwidth to 270–470 Hz, while preserving the same bandwidth in the high-frequency region. Overall, this grouping arrangement is indispensable and sufficient for addressing absorption losses in both the low-to-mid and mid-to-high frequency ranges of the proposed panel.

At the final stage of this section, all coupled unit types have been combined into a single system of nine units to examine the effect of integrating different elements in a series–parallel configuration on the overall sound absorption performance. Figure 8 describes the total sound absorption response of the inhomogeneous unoptimized supercell, consisting of 3 MPP units, 3 MPPSC units, and 3 MPPHRS units. The 3D geometries and material properties of this unoptimized sound absorbing panel (SAP) are the same as those specified earlier in Sect. 2. As shown in Fig. 8, the unoptimized SAP incorporates three double-layer MPPHRS units providing the broadest absorption at low and high frequencies combined with six single-layer MPP and MPPSC units, which help bridge absorption dips between the low-to-mid and mid-to-high frequency ranges. The absorption characteristics of the individual units have already been reported.

From the obtained results of Fig. 8, for this case, the coupled nine-unit system achieves an effective bandwidth ($\alpha \geq 0.5$) from 325 to 1600 Hz, covering 1275 Hz. Additionally, it is understandable that the sound absorbing panel (SAP) shows multiple peaks of frequency at 335 Hz ($\alpha = 0.54$), 375 Hz ($\alpha = 0.60$), 415 Hz ($\alpha = 0.60$), 490 Hz ($\alpha = 0.64$), 870 Hz ($\alpha = 0.84$), 1165 Hz ($\alpha = 0.77$), and 1600 Hz ($\alpha = 0.76$), respectively and proved numerically the concept of using the proposed fixed low perforation micro-perforated panel as a key solution to overcome low-, mid-, and high-frequency sound absorption limitations, while maintaining a compact air cavity depth of 41 mm. This reveals the strong potential of the proposed 110 × 110 mm standard square type panel, warranting further optimization to ensure optimal performance across the 300–1600 Hz range.

In addition, the resistance and reactance parts of corresponding relative acoustic impedance behaviour of each unit consistent with Fig. 8 have been illustrated in Fig. 9.(a-b). The coupled MPPHRS units exhibit a strong and narrow resonance peak due to their high acoustic impedance and

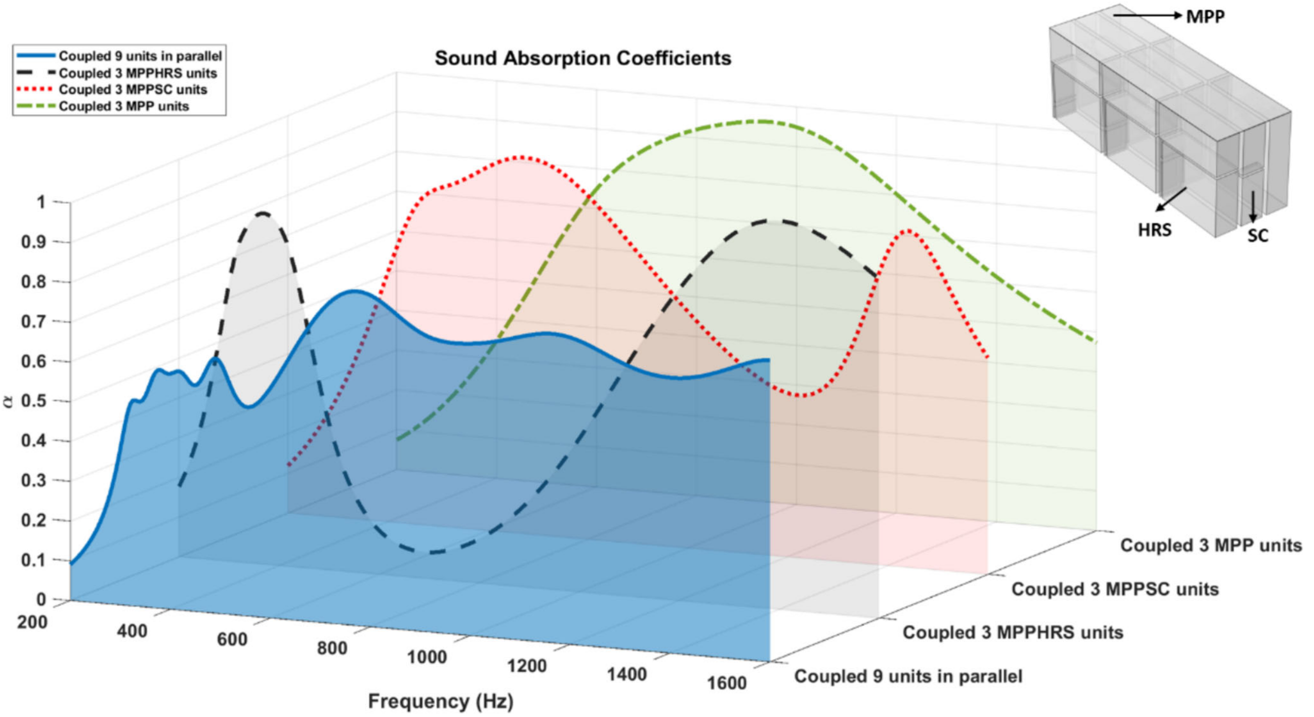

Fig. 8 Sound absorption coefficients of the unoptimized sound absorbing panel (SAP) by combination of MPP + MPPSC + MPPHRS as coupled nine units and effect of each coupled unit on the total sound absorption coefficients

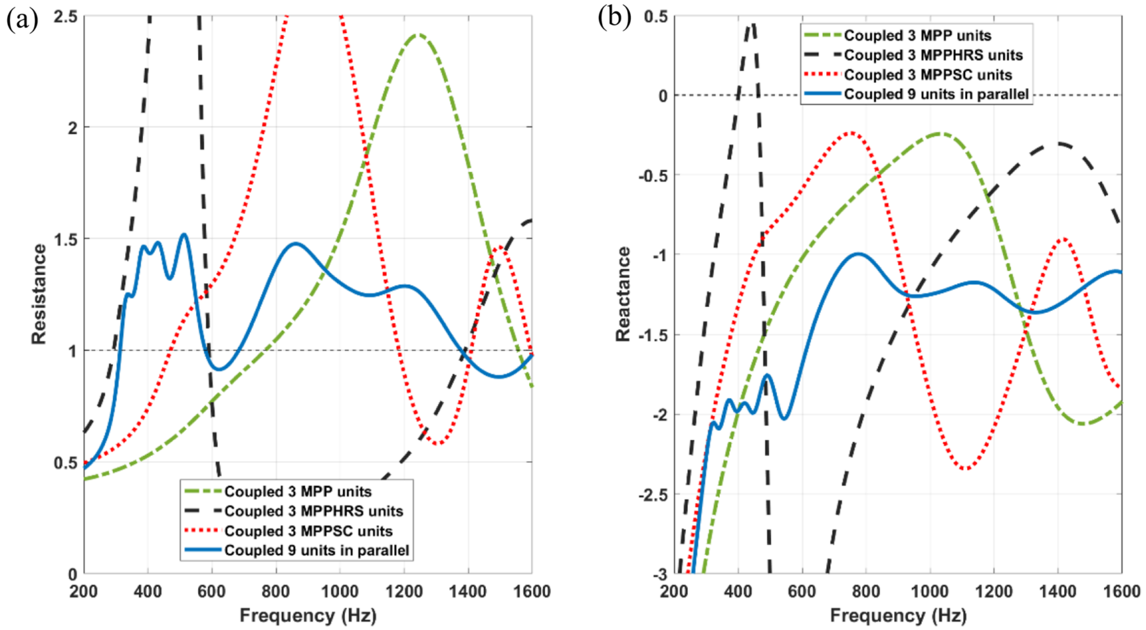

Fig. 9 Relative specific acoustic impedance of the unoptimized sound absorbing panel (SAP) consistent with Fig. 8 and their combinations: normalized resistance (**a**) and normalized reactance (**b**)

localized Helmholtz type resonance, which produces a pronounced absorption peak at 365 Hz, as observed in Fig. 8. However, when these units are integrated in parallel with the MPP and MPPSC units, the overall acoustic impedance of the system becomes the equivalent parallel combination of all individual unit impedances. As illustrated in Fig. 9 (a), the total resistance of the coupled nine-unit system remains relatively close within the range of approximately 0.75–1.5 across the 300–1600 Hz frequency band, indicating improved relatively impedance matching with the surrounding air. Meanwhile, the corresponding reactance shown in Fig. 9 (b) fluctuates more smoothly within − 2 to − 1, with significantly reduced amplitude compared to the individual units. This impedance redistribution moderates the sharp resonance behaviour of the HRS units and distributes the acoustic energy among multiple interacting resonant mechanisms provided by the MPP, MPPSC, and MPPHRS units. Consequently, the distinct high absorption peak produced by the HRS units reduced but is effectively broadened and merged into the overall broadband absorption response of the coupled system. This multi-resonant interaction enhances the overall relatively impedance matching condition over a wider frequency range, thereby producing the broadband sound absorption characteristics observed in Fig. 8.

4 Optimum Sound Absorbing Panel

The sound absorption performance of the proposed sound absorbing panel (SAP) depends on multiple variables and can be expressed as α (freq,var$_i$), where freq represents the operating frequency range, and each var$_1$, var$_2$,..., var$_i$ denotes a key adjustable design parameter, as outlined in Fig. 1 and Table 1. Manually fine-tuning these geometrical parameters to achieve the desired broadband sound absorption through parametric sweeps is often unpredictable and time-consuming. To overcome this and making sure for fine tuning the key parameters, an optimization algorithm is also employed to efficiently refine the panel design parameters for optimal performance. A genetic algorithm (GA) is a powerful optimization method belonging to the family of evolutionary algorithms, inspired by the principles of natural selection. It is widely used to solve complex optimization and search problems in engineering. The process begins with a randomly generated initial population, which evolves over successive generations. New populations are formed based on the performance of previous ones, and the evolution continues until a defined stopping criterion is met such as reaching a maximum number of generations, exceeding a time limit, or achieving a target value of the objective function [33, 50].

In this study, MATLAB's built-in 'ga' function is utilized. The algorithm starts with an initial population of 100 individuals. Tournament selection ('selectiontournament') is used to choose parents, uniform mutation ('mutationuniform') introduces variation, and crossover is performed with an 80% probability to generate offspring. The algorithm is set to terminate after 100 generations. As illustrated in Fig. 10, the study has been integrated COMSOL Multiphysics with MATLAB using the Livelink tool, enabling seamless input/output exchange through custom MATLAB scripts. The optimization process begins with the design of a parameterized sound absorbing panel (SAP) in COMSOL, then MATLAB generates the initial population for the genetic algorithm (GA). For each chromosome, the panel parameters are updated, and the sound absorption coefficient is calculated using finite element analysis (FEA) in COMSOL. The results are imported back into MATLAB, where the objective function is evaluated, and the stopping condition is checked. If the termination criterion is met, the optimization concludes. If not, a new population is generated using GA operations-selection, crossover, and mutation, and the cycle (steps 2 to 6) repeats until convergence is achieved.

To achieve the best sound absorption bandwidth within the target frequency range of 300–1600 Hz, Eq. (16) is employed as the fitness function. This approach improves overall performance by directing the optimization process specifically towards the desired frequency band [33, 50]. By setting the α_{target} to a predefined threshold (half-bandwidth,$\alpha \geq 0.5$), frequencies with absorption coefficients exceeding this value can be disregarded during optimization, this means that the higher values above than α_{target} is kept. The optimal objective function is defined as follows:

$$\begin{aligned}&\text{Objective fun: minimize, fitness}\left(\text{frequency, var}_i\right)\\&=\sum_{f_{\max}=300Hz}^{f_{\max}=1600Hz}\beta*\left(\alpha_{\text{target}}-\alpha_{\text{total}}\right),\ \beta\\&=\begin{cases}1, & \alpha_{\text{total}}<\alpha_{\text{target}}\\0, & \alpha_{\text{total}}\geq\alpha_{\text{target}}\end{cases}\end{aligned}\tag{16}$$

To simplify and focus the optimization process, constraints are applied to specific parameters of the coupled supercell such as the total height of the panel, subchannel heights, and spacing width of coiled-up spaces, as well as the aperture width and height of the HRS. Some constrained parameters are fixed according to the initial values provided in Section 2. Meanwhile, the adjustable design parameters, along with their respective lower and upper bounds, are detailed in Table 2.

4.1 Optimal Sound Absorption Performance Across a Broad Effective Bandwidth

The standard square-type sound absorbing panel (SAP) examined here demonstrates strong potential for achieving

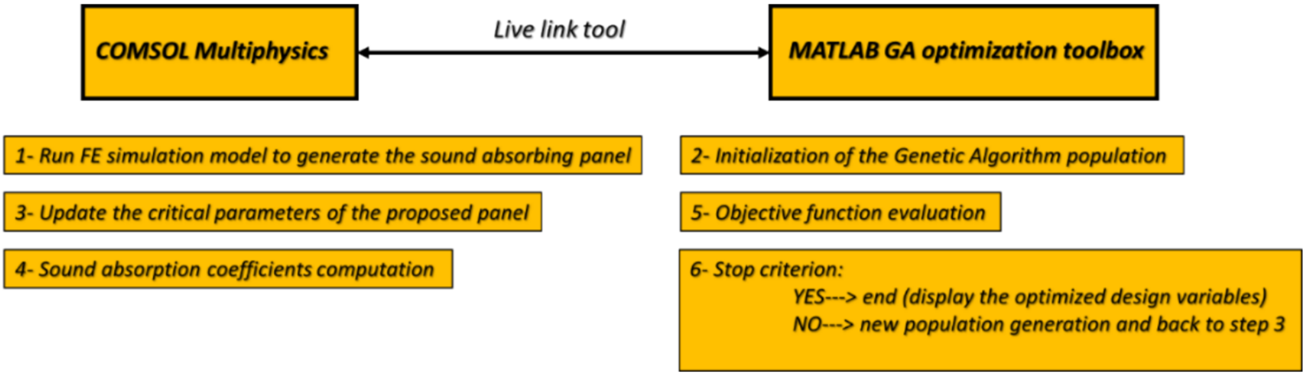

Fig. 10 GA based co-simulation optimization procedure

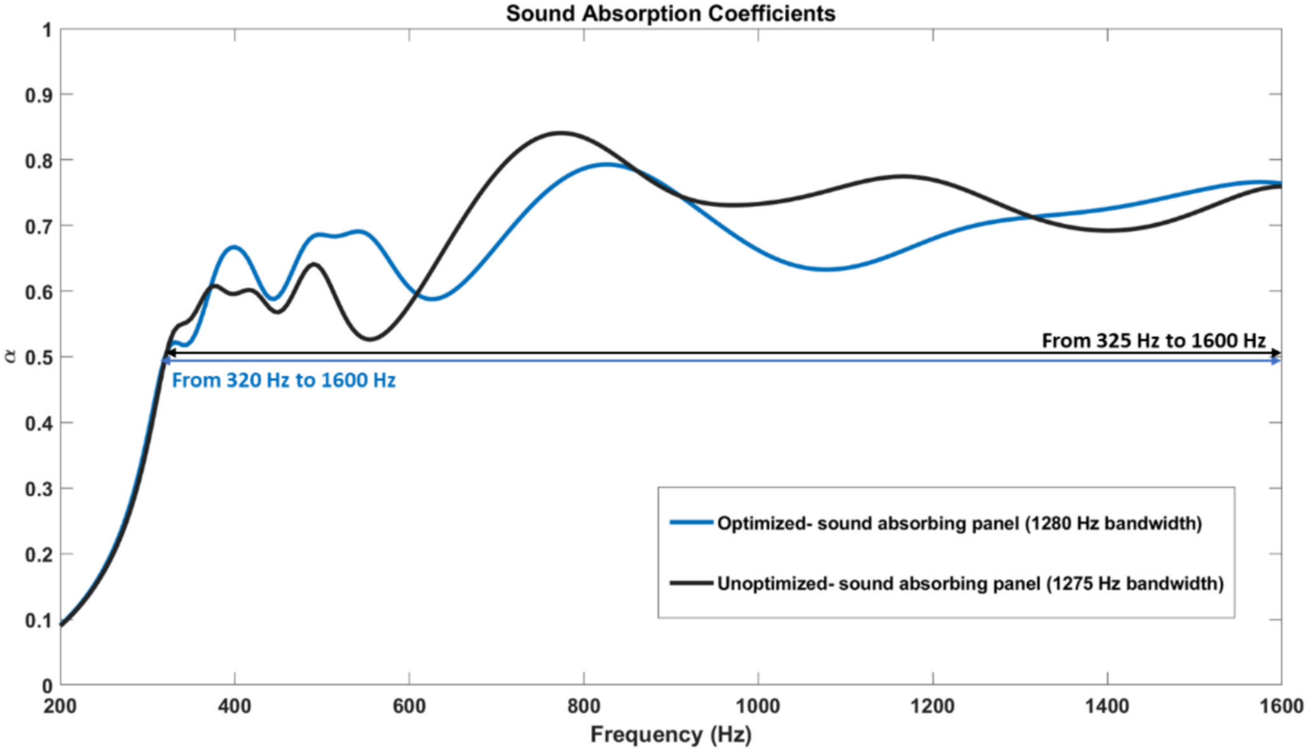

Fig. 11 Numerical sound absorption coefficients comparison of the optimized and unoptimized sound absorbing panel

a wide bandwidth, as numerically investigated in Section 3. To reach the best performance, the optimization target has been set to the 300–1600 Hz range, which is highly relevant for noise control in most engineering and industrial applications. Fig. 11 compares the sound absorption coefficients of the SAP supercell before and after optimization using a genetic algorithm (GA). Although the effective bandwidth improvement is moderate (1280 Hz compared to 1275 Hz for the unoptimized case), the optimization primarily enhances the uniformity and stability of the absorption response across the 300–1600 Hz range. In particular, the optimized configuration exhibits a smoother sound absorption curve, improved low-frequency onset behaviour, and reduced mid-frequency fluctuations, contributing to a robust broadband performance. The enhanced absorption capability of the optimized SAP comes from several resonance bands at 330 Hz ($\alpha = 0.53$), 400 Hz ($\alpha = 0.66$), 500 Hz ($\alpha = 0.70$), 540 Hz ($\alpha = 0.70$), 825 Hz ($\alpha = 0.80$), 1250 Hz ($\alpha = 0.70$), and 1600 Hz ($\alpha = 0.76$). Downward shift in the low-frequency band, along with smooth rises in absorption values, especially in the low-to-mid and mid-to-high frequency bands, are the major differences between the unoptimized and optimized cases. These improvements are a result of the optimized parameters obtained through GA-based optimization. Additional information concerning the optimized SAP is provided in Table 3, where the final design variables have been indicated.

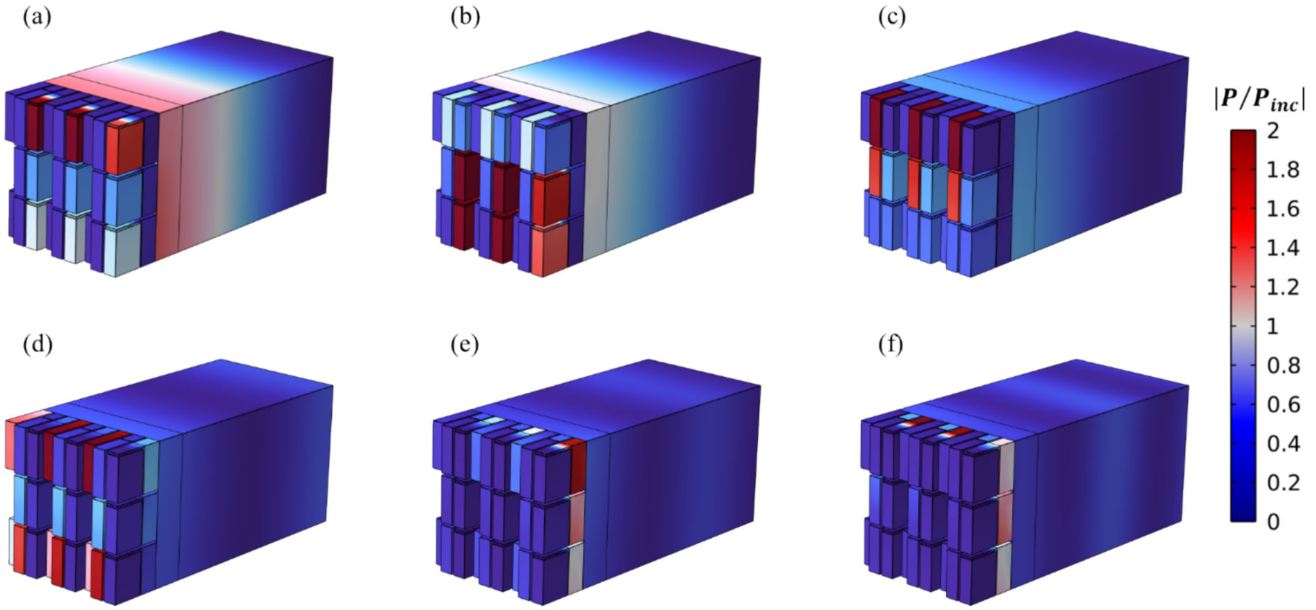

Fig. 12 Normalized acoustic pressure contours at six resonance frequencies for the Optimized sound absorbing panel: **a** 330 Hz, **b** 400 Hz, **c** 500 Hz, **d** 825 Hz, **e** 1250 Hz, **f** 1600 Hz

Table 2 Design variables of the sound absorbing panel and their lower and upper band limits in GA optimization

var_i	Lower band limit (mm)	Upper band limit (mm)
N_1	2	34
N_2	2	34
N_3	2	34
ch_1	2	36
ch_2	2	18
ch_3	2	18
ch_4	2	11
ch_5	2	11
ch_6	2	11
$d_{\mathrm{HRS\_1}}$	1	4
$d_{\mathrm{HRS\_2}}$	1	4
$d_{\mathrm{HRS\_3}}$	1	4
$h_{\mathrm{HRS\_1}}$	2	22
$h_{\mathrm{HRS\_2}}$	2	22
$h_{\mathrm{HRS\_3}}$	2	22
H_3	5	41
H_4	5	41
H_5	5	41

Table 3 Values for optimized design variable of the sound absorbing panel through the GA optimization procedure

var_i (Design variables)	Optimized values (mm)
N_1	23.30005
N_2	4.14416
N_3	12.06764
ch_1	28.04993
ch_2	6.41711
ch_3	16.06583
ch_4	8.71029
ch_5	3.78124
ch_6	4.48828
$d_{\mathrm{HRS\_1}}$	1.97533
$d_{\mathrm{HRS\_2}}$	3.01656
$d_{\mathrm{HRS\_3}}$	1.94668
$h_{\mathrm{HRS\_1}}$	10.64330
$h_{\mathrm{HRS\_2}}$	9.53822
$h_{\mathrm{HRS\_3}}$	17.47257
H_3	33.20881
H_4	19.17041
H_5	37.35462

In addition, the 3D finite element analysis (FEA) has been utilized to demonstrate the sound absorption behaviour of the optimized supercell (SAP). Fig. 12 displays the intensity contours of the non-dimensional acoustic pressure obtained from the 3D simulation. A vertically incident acoustic wave strikes the top surface of the sound absorbing panel (SAP), where p_{inc} denotes the amplitude of the incident sound pressure. Regions highlighted in red indicate areas where the units are approaching resonant state, contributing significantly to sound absorption. Specifically, Fig. 12.(a–f) displays the acoustic pressure distributions at six resonance frequencies: 330 Hz, 400 Hz, 500 Hz, 825 Hz, 1250 Hz, and 1600 Hz, respectively.

5 Experimental Measurement

5.1 Experimental Findings

To validate the accuracy of the numerical results and assess the sound absorption performance of both the optimized and unoptimized sound absorbing panel (SAP), experimental measurements were carried out in this section. The tests were conducted using the two-microphone transfer function method, following the procedures outlined in the ISO 10534-2 standard [51]. According to the ISO 10534-2 standard, the sound pressures of both the incident and reflected sound waves are determined using the following relations:

$$p_i = P_I e^{ik_0 x},\ p_r = P_R e^{-ik_0 x} \tag{17}$$

where P_I and P_R represent the amplitudes of the incident (p_i) and reflected (p_r) sound waves at the reference plane, and x denotes the position along the wave path [51]. The transfer function H_{12} can then be calculated from the analysis of the pressure responses according to the following equation:

$$H_{12} = \frac{P_2}{P_1} = \frac{e^{ikx_2} + \mathrm{R}e^{-ikx_2}}{e^{ikx_1} + \mathrm{R}e^{-ikx_1}} \tag{18}$$

where, x_1 and x_2 represent the distances from the panel to microphones 1 and 2, respectively, while P_1 and P_2 are the pressure readings measured at those two microphone positions. If s, is the spacing between the two microphones, then the reflection coefficient (R) can be determined using the following formula:

$$R = \frac{H_{12} - e^{-iks}}{e^{iks} - H_{12}} e^{2ikx_1} \tag{19}$$

And ultimately, the absorption coefficient (α) is given by:

$$\alpha = 1 - |R|^2 \tag{20}$$

As illustrated in Fig. 13. (a) and (b), the experimental setup consists of a power amplifier, a loudspeaker, two 1/4-inch microphones, and a square impedance tube with an internal cross-section of 110 × 110 mm. This setup allows for effective testing of frequencies up to 1600 Hz. The loudspeaker, driven by the amplifier, generates sound waves within the waveguide. Two microphones are placed in front of the test sample to record sound pressure, with the closest microphone positioned 250 mm from the sample surface. The test samples were manufactured using fused deposition modelling (FDM) 3D printing with PLA material, printed on a Bambu Lab P1P printer, as shown in Fig. 13. (b). The micro-perforated polyethylene film used in the panel was produced using a laser drilling process. Sealing tape was applied around the sample edges to eliminate sound leakage.

The sound absorption coefficient has been calculated from the phase and amplitude of the pressure signals recorded by the two microphones, following eq. (20). Both the unoptimized and optimized samples were measured, and their experimental and numerical results are compared in Fig. 13. (c).

The experimental records in Fig. 13 (c) explore two clearly different sound absorption performances between the unoptimized and optimized panels. For the unoptimized panel, the sound absorption coefficient is larger than 0.5 between 350–1600 Hz, and the respective effective bandwidth is 1250 Hz. This is somewhat different from the numerical simulation, however, where the 0.5 threshold was found at 325 Hz, 25 Hz below that of the experiment result. In addition, the experimental result for this case has revealed prominent peaks at 370 Hz ($\alpha = 0.54$), 400 Hz ($\alpha = 0.56$), 500 Hz ($\alpha = 0.62$), 775 Hz ($\alpha = 0.76$), 1000 Hz ($\alpha = 0.79$), and 1600 Hz ($\alpha = 0.68$). In contrast, the optimized case demonstrated improved low-frequency performance, achieving sound absorption coefficients above 0.5 across the range of 345–1600 Hz, resulting in an extended bandwidth of 1255 Hz. Numerical simulations of the optimized panel showed close agreement with the experimental results, with only a 25 Hz deviation at the starting point, which the calculated sound absorption threshold began at 320 Hz instead of 345 Hz.

Correspondingly, for the optimized case dominant peaks in the experimental result have been identified at 345 Hz ($\alpha = 0.50$), 400 Hz ($\alpha = 0.61$), 500 Hz ($\alpha = 0.67$), 825 Hz ($\alpha = 0.73$), 1210 Hz ($\alpha = 0.72$), and 1600 Hz ($\alpha = 0.67$). Both test samples exhibited absorption coefficients above 0.5 within the target frequency range according to the experimental results. All in all, the experimental trends aligned closely with the simulations, with minor discrepancies in their magnitude likely caused by fabrication and assembly imperfections, as well as the idealized assumptions used in the numerical calculation.

5.2 Experimental Comparison Results of the SAP with Existing Works

A normalized metric for evaluating the efficiency of broadband sound absorber panels was introduced in [52, 53] , defined as the bandwidth-to-thickness ratio. This measure is calculated by summing the frequency ranges where the sound absorption coefficient exceeds 0.5, then dividing that

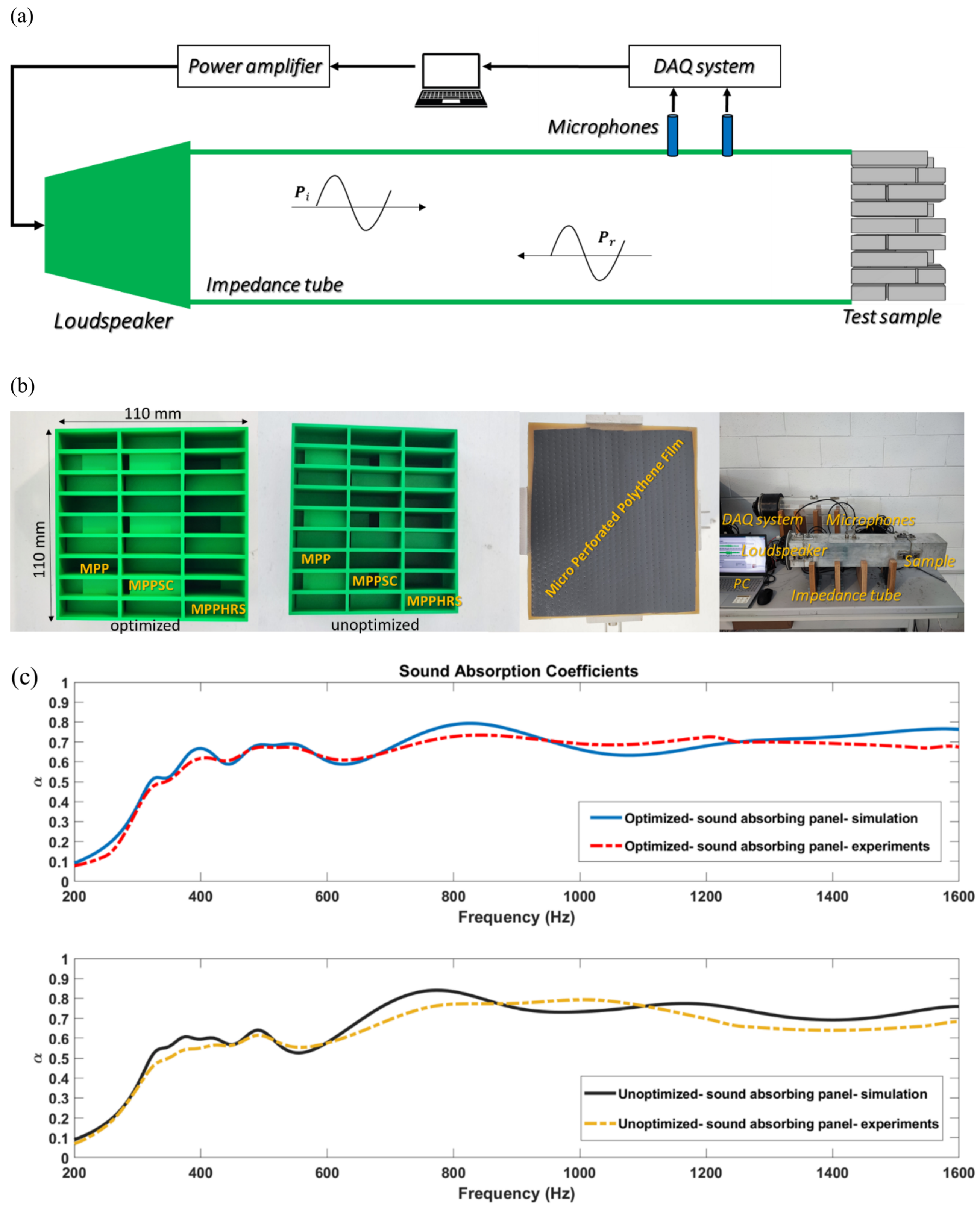

Fig. 13 Experimental realization of the sound absorption characteristics of the sound absorbing panel (SAP): **a** Schematic of the sound absorption measurement system, **b** photographs of the test sample and measurement setup, **c** numerical and experimental comparison on sound absorption spectrum of the sound absorbing panel (SAP)

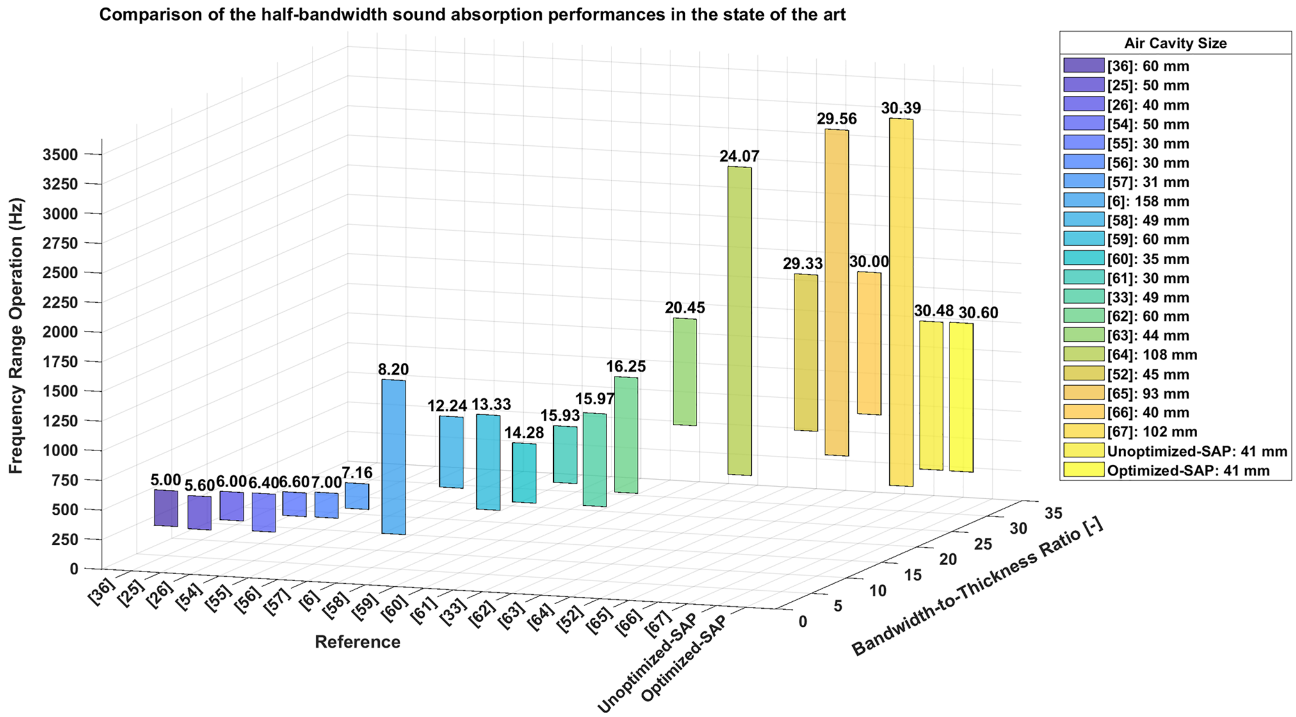

Fig. 14 Comparison of the sound absorption performances of the sound absorbing panel (SAP) with available literature

total bandwidth by the thickness of the panel's air cavity. In this study, the same metric is adopted to assess the performance of the proposed absorber design based on experimental results, as it effectively quantifies sound absorption efficiency per unit thickness. To benchmark the performance of the proposed panel, Fig. 14 presents a comparison of the achieved bandwidth-to-thickness ratios against those reported in state-of-the-art designs employing various sound absorption mechanisms. The results exhibit that both the unoptimized and optimized versions of the thin meta-absorber developed in this work achieved higher ratios 30.48 and 30.60, respectively, and surpassing those of existing sound absorption panels. This improvement demonstrates the superior efficiency of the proposed design in delivering broadband sound absorption with minimal thickness and a fixed low perforation rate, highlighting its advantages over previously reported solutions [54–67].

6 Conclusion

This study has focused on the design, optimization, and experimental validation of a new sound-absorbing panel composed of single- and double-layer elements. The elements are based on micro-perforated panels (MPPs) combined with conventional channels, space-coiling and Helmholtz resonator slit-type (HRS) structures, specifically developed to achieve broadband low-frequency sound absorption. By means of systematic finite element simulations, the hybrid series–parallel configuration was proposed, consisting of nine integrated units: three double-layer units with MPP–HRS series configurations, coupled in parallel with six single-layer MPP units backed by normal and coiled-up space channels. This arrangement strategically induces multiple resonance peaks, enhancing absorption across low, mid, and high-frequency ranges. To further improve performance, a genetic algorithm was employed to optimize key geometric parameters, enhancing absorption bandwidth while maintaining a compact thickness. Experimental impedance tube measurements confirmed the numerical simulations, showing effective absorption bandwidths of 1250 Hz for the unoptimized design and 1255 Hz for the optimized design, both with an air cavity depth of 41 mm. The unoptimized and optimized panels achieved bandwidth-to-thickness ratios of 30.48 and 30.60, respectively, demonstrating high absorption efficiency per unit thickness while employing a fixed low perforation rate. The selected total thickness of 41 mm represents a deliberate balance between low-frequency resonance tuning and structural compactness, enabling subwavelength broadband absorption down to 345 Hz and offering a practical alternative to conventional absorbers that require significantly greater thickness in this frequency range. Owing to its modular series–parallel architecture, the proposed panel can be tailored to selectively target narrower frequency ranges through geometric adjustment or modification of specific unit components; however, such customization would involve trade-offs in bandwidth, thickness, and structural complexity. In the present study, the configuration was intentionally optimized to maximize broadband performance relative to thickness, as quantified by the bandwidth-to-thickness ratio. Future investigations will focus on evaluating the performance of the proposed panel under oblique and diffuse field incidence conditions, as well as exploring multi-objective optimization strategies and scalability for practical large-area implementations.

Author Contribution Emad Panahi: conceptualization, methodology, data curation, investigation, software, validation, visualization, writing-original draft, writing-review and editing. Francesco Braghin: investigation, project administration, supervision, writing-review and editing. Alberto Corigliano: investigation, project administration, supervision, writing-review&editing. Luca Sangiuliano: investigation, project administration, supervision, writing-review&editing. Luca D'Alessandro: investigation, project administration, supervision, writing-review&editing.

Declarations

Conflict of interest The authors declare that they have no known competing financial interests or personal relationships that could have appeared to influence the work reported in this paper.

References

1. Rafique, F., Wu, J.H., Naqvi, S.M.A., Ma, F.: Enhanced wideband low-frequency sound absorption of a single-layer multiple parallel-arranged inhomogeneous microperforated panel absorber. Acoust. Aust. **50**, 49–69 (2022). https://doi.org/10.1007/s40857-021-00252-3
2. Tao, Y., Ren, M., Zhang, H., Peijs, T.: Recent progress in acoustic materials and noise control strategies–a review. Appl. Mater. Today **1**(24), 101141 (2021)
3. Diao, W., Pei, N., Fan, L., Zhang, S., Cheng, L., Xu, X.: A composite sound insulator composed of a helix and a resonator array. Acoust. Aust. **53**, 419–427 (2025). https://doi.org/10.1007/s40857-025-00359-x
4. Yang, M., Sheng, P.: Sound absorption structures: from porous media to acoustic metamaterials. Annu. Rev. of Mater. Res. **3**(47), 83–114 (2017)
5. Zhang, J., Hu, B., Wang, S.: Review and perspective on acoustic metamaterials: from fundamentals to applications. Appl. Phys. Lett. (2023). https://doi.org/10.1063/5.0152099
6. Prasetiyo, I., Sihar, I., Sudarsono, A.S.: Realization of a thin and broadband microperforated panel (MPP) sound absorber. Appl. Acoust. (2021). https://doi.org/10.1016/j.apacoust.2021.108295
7. Shafeer P.P, M., Pitchaimani, J., Doddamani, M.: 3D printed thick micro-perforated panel with graded perforation for practical wall sound absorption applications. Acoust. Aust. **52**, 25–40 (2023). https://doi.org/10.1007/s40857-023-00303-x
8. Maa, D.Y.: Microperforated-panel wideband absorbers. Noise Control Eng. J. **29**(3), 77 (1987)
9. Maa, D.-Y.: Potential of microperforated panel absorber. J. Acoust. Soc. Am. 104, (1998). https://doi.org/10.1121/1.423870i
10. Sakagami, K., Matsutani, K., Morimoto, M.: Sound absorption of a double-leaf micro-perforated panel with an air-back cavity and a rigid-back wall: detailed analysis with a Helmholtz-Kirchhoff integral formulation. Appl. Acoust. **71**, 411–417 (2010). https://doi.org/10.1016/j.apacoust.2009.11.014
11. Ruiz, H., Cobo, P., Jacobsen, F.: Optimization of multiple-layer microperforated panels by simulated annealing. Appl. Acoust. **72**, 772–776 (2011). https://doi.org/10.1016/j.apacoust.2011.04.010
12. Cobo, P., de la Colina, C., Roibás-Millán, E., Chimeno, M., Simón, F.: A wideband triple-layer microperforated panel sound absorber. Compos. Struct. (2019). https://doi.org/10.1016/j.compstruct.2019.111226
13. Bucciarelli, F., Malfense Fierro, G.P., Meo, M.: A multilayer microperforated panel prototype for broadband sound absorption at low frequencies. Appl. Acoust. **146**, 134–144 (2019). https://doi.org/10.1016/j.apacoust.2018.11.014
14. Zhao, L., Lin, T.R.: A turned double-layer microperforated panel for low frequency sound absorption in enclosures with limited cavity space. Appl. Acoust. (2022). https://doi.org/10.1016/j.apacoust.2021.108594
15. Wang, J., Bennett, G.J.: Ultra-broadband sound absorption in a compact multi-chamber micro-perforated panel absorber with varying depths. AIP Adv. (2024). https://doi.org/10.1063/5.0187328
16. Xiang, N., Fackler, C.J., Hou, Y., Schmitt, A.A.J.: Bayesian design of broadband multilayered microperforated panel absorbers. J. Acoust. Soc. Am. (2022). https://doi.org/10.1121/10.0007224
17. Zhou, Z., Huang, S., Li, D., Zhu, J., Li, Y.: Broadband impedance modulation via non-local acoustic metamaterials. Natl. Sci. Rev. (2022). https://doi.org/10.1093/nsr/nwab171
18. Bi, S., Wang, E., Shen, X., Yang, F., Zhang, X., Yang, X., Yin, Q., Shen, C., Xu, M., Wan, J.: Enhancement of sound absorption performance of Helmholtz resonators by space division and chamber grouping. Appl. Acoust. (2023). https://doi.org/10.1016/j.apacoust.2023.109352
19. Rafique, F., Wu, J.H., Liu, C.R., Ma, F.: Low-frequency sound absorption of an inhomogeneous micro-perforated panel with J-shaped cavities of different depths. Acoust. Aust. **50**, 203–214 (2022). https://doi.org/10.1007/s40857-021-00261-2
20. Ren, Z., Cheng, Y., Chen, M., Yuan, X., Fang, D.: A compact multifunctional metastructure for low-frequency broadband sound absorption and crash energy dissipation. Mater. Des. **215**, 110462 (2022). https://doi.org/10.1016/j.matdes.2022.110462
21. Li, S., Sun, Y., Han, Q., Li, C.: Sound absorption and enhancement mechanism of hierarchical slit-embedded Helmholtz resonators. Smart Mater. Struct. (2025). https://doi.org/10.1088/1361-665X/adab58
22. Xu, C., Sun, Y., Shi, M., Mao, Y.: Ultra-low frequency sound absorber combining quasi-zero-stiffness structure and Helmholtz resonator. Aerosp. Sci. Technol. **167**, 110688 (2025). https://doi.org/10.1016/j.ast.2025.110688
23. Liang, J., Liu, Z., Wang, Q., Zhao, Y., Fard, M., Davy, J.L.: Optimization of the acoustic performance of a composite multi-cell sound absorber. Acoust. Aust. **51**, 319–333 (2023). https://doi.org/10.1007/s40857-023-00297-6
24. Cheng, B., Gao, N., Zhang, R., Hou, H.: Design and experimental investigation of broadband quasi-perfect composite loaded sound absorber at low frequencies. Appl. Acoust. **178**, 108026 (2021). https://doi.org/10.1016/j.apacoust.2021.108026
25. Xu, W., Liu, J., Yu, D., Wen, J.: Coherent coupling based metastructures for high acoustic absorption at 220–500 Hz frequency. Appl. Acoust. (2021). https://doi.org/10.1016/j.apacoust.2021.108181
26. Zeng, K., Li, Z., Guo, Z., Liang, X., Wang, Z.: Acoustic metamaterial for highly efficient low-frequency impedance modulation by extensible design. Extreme Mech. Lett. (2022). https://doi.org/10.1016/j.eml.2022.101855
27. Chen, X., Sun, F., Zhang, J., Chen, G., Xu, L., Fan, L., Cheng, L., Xu, X., Chen, Y., Zhou, J., Li, L., Yang, S.: A compact acoustic

metamaterial based on Helmholtz resonators with side slits for low-frequency sound absorption. Appl. Phys. Lett. (2024). https://doi.org/10.1063/5.0212688

28. Liu, C.R., Wu, J.H., Yang, Z., Ma, F.: Ultra-broadband acoustic absorption of a thin microperforated panel metamaterial with multi-order resonance. Compos. Struct. (2020). https://doi.org/10.1016/j.compstruct.2020.112366
29. Liu, L., Chang, H., Zhang, C., Hu, X.: Single-channel labyrinthine metasurfaces as perfect sound absorbers with tunable bandwidth. Appl. Phys. Lett. (2017). https://doi.org/10.1063/1.4986142
30. Cai, X., Guo, Q., Hu, G., Yang, J.: Ultrathin low-frequency sound absorbing panels based on coplanar spiral tubes or coplanar Helmholtz resonators. Appl. Phys. Lett. (2014). https://doi.org/10.1063/1.4895617
31. do N. Almeida, G., Vergara, E.F., Barbosa, L.R., Lenzi, A., Mareze, P.H., Birch, R.S.: Acoustic analysis of a metasurface for normal and random incidence sound waves. Phys. Lett. A **451**, 128417 (2022). https://doi.org/10.1016/j.physleta.2022.128417
32. Wang, Y., Yuan, H., Wang, Y., Xu, J., Yu, H., Zhang, C., Ren, L.: A study on ultra-thin and ultra-broadband acoustic performance of micro-perforated plate coupled with coiled-up space structure. Appl. Acoust. (2022). https://doi.org/10.1016/j.apacoust.2022.109048
33. Xiang, L., Wang, G., Luo, G., Shen, J., Deng, Z., Wen, S.: Optimization of hybrid microperforated panel and nonuniform space-coiling channels for broadband low-frequency acoustic absorption. Appl. Acoust. (2024). https://doi.org/10.1016/j.apacoust.2023.109763
34. Qian, Y., Li, B., Zhang, J.: Study of ultra-wideband acoustic metamaterial based on multi-order broadband resonance band coupling of ultra-micro perforated panel. Appl. Acoust. (2025). https://doi.org/10.1016/j.apacoust.2025.110643
35. Zheng, M., Chen, C., Li, X.: Ultra-broadband and nonlinear robust sound absorption based on ultra-microperforated panel. J. Sound Vib. (2024). https://doi.org/10.1016/j.jsv.2024.118262
36. Guo, J., Zhang, X., Fang, Y., Jiang, Z.: Wideband low-frequency sound absorption by inhomogeneous multi-layer resonators with extended necks. Compos. Struct. (2021). https://doi.org/10.1016/j.compstruct.2020.113538
37. Liu, C.R., Wu, J.H., Ma, F., Chen, X., Yang, Z.: A thin multi-order Helmholtz metamaterial with perfect broadband acoustic absorption. Appl. Phys. Express **12**, 084002 (2019). https://doi.org/10.7567/1882-0786/ab2f94
38. Zhu, J., Qu, Y., Su, H., Zhang, J., Meng, G.: A multi-layer overlapping structure for continuous broadband acoustic wave absorption at lower-frequencies. Appl. Acoust. **187**, 108496 (2022). https://doi.org/10.1016/j.apacoust.2021.108496
39. McKay, A., Davis, I., Killeen, J., Bennett, G.J.: SeMSA: a compact super absorber optimised for broadband, low-frequency noise attenuation. Sci. Rep. **10**, 17967 (2020). https://doi.org/10.1038/s41598-020-73933-0
40. Hu, G., Tang, L., Cui, X.: On the modelling of membrane-coupled Helmholtz resonator and its application in acoustic metamaterial system. Mech. Syst. Signal Process. **132**, 595–608 (2019). https://doi.org/10.1016/j.ymssp.2019.07.017
41. Xu, Q., Qiao, J., Ren, Z., Sun, J., Zhang, G., Li, L.: Multi synergistic coupling design for broadband sound absorption based on compact porous composite embedded with massless membrane resonator. Compos. Struct. **286**, 115312 (2022). https://doi.org/10.1016/j.compstruct.2022.115312
42. Vergara, E.F., Almeida, G.N., Barbosa, L.R., Lenzi, A., Carvalho de Sousa, A.: Broadband and low-frequency sound absorption of modified Helmholtz resonator combined with porous layer addition. J. Appl. Phys. (2022). https://doi.org/10.1063/5.0108807
43. Park, S.H.: Acoustic properties of micro-perforated panel absorbers backed by Helmholtz resonators for the improvement of low-frequency sound absorption. J. Sound Vib. **332**, 4895–4911 (2013). https://doi.org/10.1016/j.jsv.2013.04.029
44. Gai, X.-L., Xing, T., Li, X.-H., Zhang, B., Wang, W.-J.: Sound absorption of microperforated panel mounted with Helmholtz resonators. Appl. Acoust. **114**, 260–265 (2016). https://doi.org/10.1016/j.apacoust.2016.08.001
45. Mahesh, K., Mini, R.S.: Theoretical investigation on the acoustic performance of Helmholtz resonator integrated microperforated panel absorber. Appl. Acoust. **178**, 108012 (2021). https://doi.org/10.1016/j.apacoust.2021.108012
46. Li, H., Wu, J., Yan, S., Mao, Q.: Design and study of broadband sound absorbers with partition based on micro-perforated panel and Helmholtz resonator. Appl. Acoust. **205**, 109262 (2023). https://doi.org/10.1016/j.apacoust.2023.109262
47. Yang, X., Wang, E., Shen, X., Peng, W., Zhu, D., Song, H., Hu, D., Shen, C., Xu, M., Li, Z., Shi, Q.: Multilayer stackable grouped acoustic metamaterial with optional sound absorption performance. J. Appl. Phys. (2025). https://doi.org/10.1063/5.0254856
48. Panahi, E., Braghin, F., Corigliano, A., Sangiuliano, L., D'Alessandro, L.: Thin meta-absorber for low-frequency broadband sound absorption: design, optimization, and experiments. Mech. Adv. Mater. Struct. **33**(1), 2637872 (2026)
49. Beltman, W.M., Van der Hoogt, P.J., Spiering, R.M., Tijdeman, H.: IMPLEMENTATION AND EXPERIMENTAL VALIDATION OF A NEW VISCOTHERMAL ACOUSTIC FINITE ELEMENT FOR ACOUSTO-ELASTIC PROBLEMS. J. Sound Vib. **216**(1), 159–185 (1998)
50. Panahi, E., Braghin, F., Corigliano, A., Sangiuliano, L., D'Alessandro, L.: Compacted meta-panel through inhomogeneous double layer micro perforated and coiled up space channels for a broadband sound absorption: FEM based optimization and experiments. Appl. Acoust. **248**, 111276 (2026). https://doi.org/10.1016/j.apacoust.2026.111276
51. ISO 10534–2:2023 Acoustics—determination of acoustic properties in impedance tubes Part 2: two-microphone technique for normal sound absorption coefficient and normal surface impedance
52. Liu, Y., Zeng, X., Ren, S., Sun, W., Wang, H., Lei, Y.: A broadband multi-resonant sound-absorbing metastructure based on impedance-matching nesting channels. Appl. Acoust. (2024). https://doi.org/10.1016/j.apacoust.2024.110099
53. Wang, Y., Chen, W., Liu, S.: Optimal ultra-broadband sound-absorption performance design for coiled up space structures with nonlinear robustness. Appl. Acoust. (2025). https://doi.org/10.1016/j.apacoust.2024.110236
54. Yan, X., Liang, Q., Feng, J., He, J., Fu, R., Li, D., Chen, T.: Design and manufacture of low-frequency acoustic absorption metamaterials with enhanced coupling characteristic. Virtual Phys. Prototyp. (2024). https://doi.org/10.1080/17452759.2024.2383297
55. Yang, X., Wen, G., Jian, L., Lin, C., He, J., Sedaghati, R., Huang, S., Liu, J., Min Xie, Y.: Archimedean spiral channel-based acoustic metasurfaces suppressing wide-band low-frequency noise at a deep subwavelength. Mater. Des. (2024). https://doi.org/10.1016/j.matdes.2024.112703
56. Wang, X., Qin, R., Lu, J., Huang, M., Zhang, X., Chen, B.: Laser additive manufacturing of hierarchical multifunctional chiral metamaterial with distinguished damage-resistance and low-frequency broadband sound-absorption capabilities. Mater. Des. (2024). https://doi.org/10.1016/j.matdes.2024.112659
57. Wang, X., Yu, C., Xin, F.: Tunable acoustic metamaterial for broadband low-frequency sound absorption by continuous acoustic impedance manipulation. J. Vib. Control (2024). https://doi.org/10.1177/10775463241235783

58. Liu, Q., Yang, J.S., Tang, Y.Y., Li, H.Z., Xu, Y.Y., Liu, X.C., Li, S., Yin, P.: A multi-layered corrugated resonator acoustic metamaterial with excellent low-frequency broadband sound absorption performance. Appl. Acoust. (2024). https://doi.org/10.1016/j.apacoust.2023.109800
59. Zhu, X., Weng, H., Ding, Q., Liu, Y., Li, M., Lu, X.: Design and optimization of low-frequency broadband acoustic absorption structures based on multi-cellular element co-coupling. Appl. Acoust. (2024). https://doi.org/10.1016/j.apacoust.2024.110098
60. Ryoo, H., Yong Lee, K., Jeon, W.: Broadband sound absorption using hybrid resonators with embedded necks and micro-perforations in parallel. Mech. Syst. Signal Process. (2024). https://doi.org/10.1016/j.ymssp.2024.111205
61. Kong, W., Fu, T., Rabczuk, T.: Improvement of broadband low-frequency sound absorption and energy absorbing of arched curve Helmholtz resonator with negative Poisson's ratio. Appl. Acoust. (2024). https://doi.org/10.1016/j.apacoust.2024.110011
62. Liu, C.R., Wu, J.H., Chen, X., Ma, F.: A thin low-frequency broadband metasurface with multi-order sound absorption. J. Phys. D Appl. Phys. (2019). https://doi.org/10.1088/1361-6463/aafaa3
63. Meng, D., Li, L., Wu, Z.: Helmholtz resonator-based acoustic metamaterials enabling broadband asymmetric sound absorption and ventilation. J. Low Freq. Noise Vib. Act. Control **42**, 1242–1250 (2023). https://doi.org/10.1177/14613484231151273
64. Yang, M., Chen, S., Fu, C., Sheng, P.: Optimal sound-absorbing structures. Mater. Horiz. **4**(4), 673–680 (2017)
65. Liu, C., Yang, Z., Liu, X., Wu, J.H., Ma, F.: Ultra-broadband acoustic absorption with inhomogeneous high-order Fabry-Pérot resonances. APL Mater. (2023). https://doi.org/10.1063/5.0174013
66. Agarwalla, D.K., Mohanty, A.R.: Broadband sound absorption technique using micro-perforated panel absorber with perforated extended panel. J. Vib. Eng. Technol. **12**, 495–511 (2024). https://doi.org/10.1007/s42417-023-00855-2
67. Liu, C., Liu, X., Xie, Z., Wu, J.H., Ma, F.: A tunable high-order micro-perforated panel metamaterial with low-frequency broadband acoustic absorption. Appl. Phys. Express (2024). https://doi.org/10.35848/1882-0786/ad6956